POLITECNICO
MILANO 1863

SCUOLA DI INGEGNERIA INDUSTRIALE
E DELL'INFORMAZIONE

Uncertainty quantification for in-flight icing collection efficiency in SLD conditions

Tesi di Laurea Magistrale in
Aeronautical Engineering - Ingegneria Aeronautica

Author: **Gabriele Veluti**

Student ID: 905754
Advisor: Prof. Alberto Matteo Attilio Guardone
Co-advisor: Ing. Tommaso Bellosta
Academic Year: 2020-21

Abstract

During the flight of an aircraft, the formation of ice on the surfaces represents one of the main concerns; consequently, its prevention and management play a crucial role in aircraft design and safety requirements. The water collected on the surfaces could freeze during a flight in cold wet air, bringing to a degradation of the aerodynamic performances or compromising the controllability of the aircraft, and therefore, the safety of the passengers. The design of a reliable ice protection system requires a deep knowledge of the physics of ice accretion and accurate predictions from numerical model employed. However, the reliability of numerical models is affected by the uncertainty deriving from not only the computational framework, but also the environmental conditions: indeed, these are retrieved from the experimental setup, and therefore, affected by the uncertainty. In this context, the focus of this thesis is to investigate the collection efficiency under parametric uncertainty and extend current uncertainty quantification approaches for Supercooled Large Droplets (SLD) regime. The latter has a more complex physics since the particles of water present in the cloud can deform under aerodynamic force and, moreover, they can splash or rebound when impinging the surfaces. To assess the principal statistical moments related with the numerical solutions, the uncertain input parameters are forward propagated in the computational framework using the Polynomial Chaos Expansion (PCE) method. In the presented work, diverse initial conditions and two different two-dimensional aeronautical geometries are considered with the aim to reproduce the experimental data carried out at NASA's Glenn Icing Research Tunnel (IRT). The study is performed considering test conditions related to the Appendix-C and Appendix-O of Federal Aviation Administration (FAA) airworthiness standard. This work aims at quantifying the sensitivity of the predicted collection efficiency in uncertain test conditions with a twofold objective. On one hand, the aim is to shed light on the physics by exposing the relative importance of the diverse uncertain inputs to the resulting quantity of interest. On the other hand, this work is also meant to be an embryonic effort towards assessing the accuracy of numerical predictions against uncertain observations.

Keywords: Ice accretion, SU2, PoliDrop, splash model, Supercooled Large Droplets (SLD), Polynomial Chaos Expansion (PCE), uncertainty quantification.

Abstract in lingua italiana

La formazione di ghiaccio su un velivolo rappresenta una delle maggiori problematiche durante il volo; essa ricopre quindi un ruolo chiave nei requisiti di sicurezza. L'acqua raccolta sulle superfici può ghiacciare quando il velivolo vola in condizioni esterne di aria fredda e umida, causando un peggioramento delle performance aerodinamiche; nei casi peggiori, può inoltre comportare la perdita di controllo del velivolo e mettere a rischio la sicurezza dei passeggeri. Il design dei sistemi di protezione dal ghiaccio richiede quindi una profonda conoscenza della fisica di accrescimento e i modelli numerici che vengono sviluppati devono accuratamente prevederne la forma. Tuttavia, l'affidabilità dei modelli numerici è messa in discussione dall'incertezza derivante non solo dal contesto computazionale, ma anche dalle condizioni ambientali; questi ultimi sono recuperati dal setup di laboratorio in letteratura e sono affetti da incertezza strumentale. In questo contesto, l'obiettivo della tesi è di investigare il calcolo della collection efficiency considerando l'incertezza parametrica ed estendere gli attuali approcci di quantificazione d'incertezza al regime di Supercooled Large Droplets (SLD). Quest'ultimo presenta una fisica più complessa da modellare in quanto le particelle d'acqua presenti nelle nubi possono deformarsi sotto l'azione delle forze aerodinamiche e, inoltre, possono avvenire fenomeni di splash o rebound durante l'impatto con il velivolo. Per calcolare i principali momenti statistici, e quindi propagare in avanti l'incertezza dei parametri di input, è stato utilizzato il metodo dell'Espansione in Caos Polinomiale (PCE). In questo lavoro sono stati presi in considerazione due profili aeronautici e diverse condizioni iniziali con l'obiettivo di riprodurre i dati sperimentali raccolti dal Glenn Icing Research Tunnel (IRT) della NASA. Sono state considerate diverse condizioni di input relative sia all'Appendice-C sia all'Appendice-O degli standard di idoneità al volo definiti dalla Federal Aviation Administration (FAA). L'obiettivo di questo lavoro è quantificare la sensitività della collection efficiency predetta dalle simulazioni numeriche rispetto alle condizioni sperimentali incerte. Lo scopo è duplice: da una parte si vuole fare luce sulla fisica dell'accrescimento del ghiaccio esponendo l'importanza sulle quantità d'interesse dei diversi input affetti da incertezza. Dall'altra parte, questa tesi è anche un primo tentativo di valutare l'accuratezza di una predizione numerica rispetto alle osservazioni incerte.

Parole chiave: Accrescimento del ghiaccio, Polidrop, SU2, Supercooled Large Droplets (SLD), espansione in caos polinomiale, quantificazione d'incertezza.

Contents

List of Figures

List of Tables

List of Symbols

Variable	Description	SI unit
AoA	Angle of Attack	
CFD	Computational Fluid Dynamics	
FAA	Federal Aviation Administration	
IPS	Ice Protection System	
IRT	Glenn Icing Research Tunnel	
LE	Leading edge	
LHS	Latin Hypercube Sampling	
LS	Least Square approach	
LWC	Liquid Water Content	g/m^3
MCS	Monte Carlo Sampling	
MVD	Median Value Diameter	μm
PCE	Polynomial Chaos Expansion	
$RANS$	Raynolds Averaged Navier-Stokes equations	
$RMSE$	Root Mean Square Error	
SLD	Supercooled Large Droplet	
SST	Shear-Stress Transport model	
UQ	Uncertainty Quantification	
α_{imp}	Impingement angle of the droplets	
β	Collection Efficiency	
δ	Correction factor	
δy	Separation of the trajectories in the freestream	m
δs	Separation between trajectories when impact the surface	m
ϵ	Dissipation ratio	m^2/s^3
ξ	Set of random variables	
μ	Dynamic viscosity	$kg/m \cdot s$

ρ	Density	kg/m^3
σ	Standard deviation	
σ^2	Variance	
Ψ	Random polynomial basis	
ω	Characteristic frequency of the eddies	s^{-1}
a	Polar axis	
c	Equatorial axis	
c_k	Polynomial expansion coefficients	
C	Chord of the airfoil	m
C_D	Drag coefficient	
C_L	Lift coefficient	
C_p	Local pressure coefficient	
dA_∞	Area upstream	m^2
dA_i	Area at the surface	m^2
d_p	Particle diameter	m
f	Eccentricity function	
F_a	Aerodynamic forces	N
fr_*	Dimentionless drop frequency	
He	Hermite polynomials	
k	Turbulence kinetic energy	m^2/s^2
K	Splashing threshold	
$K_{L,n}$	Splashing threshold in LEWICE model	
m_p	Mass of the particle	kg
Oh	Ohnesorge number	
Re	Reynolds number	
Re_p	Particle Reynolds number	
S_u	Sobol indices	
u_∞	Freestream Velocity	m/s
$\mathbf{u_f}$	Flow velocity	m/s
$\mathbf{u_p}$	Particle velocity	m/s
V_n	Normal velocity of the droplets	m/s
V_t	Tangential velocity of the droplets	m/s
x_0	Particle initial position	m

x_p	Particle displacement	m
y^+	Dimentionless wall distance	
We	Weber number	
We_b	Breakup Weber number	

1 Introduction

One of the main concerns during the flight of an aircraft is the formation of ice on its surfaces, which can lead to a worsening of the aerodynamic performances [1]: the passive drag increases, as does the weight, resulting in more fuel consumption; at the same time, the lift and the stall angle can considerably decrease. The ice formation can also impact the aeroelastic stability and control of the aircraft, especially if it takes place on the manoeuvring surfaces or in the external sensor [2], leading to a lack of control and safety. It can not only occur on the external surface, but also in the nacelle of the engine or in the rotating surfaces, hence, altering the flow at the inlet and possibly causing an unbalanced load or shedding phenomena [3]. For these reasons, icing is a fundamental point of the safety regulations, and plays a crucial role in aircraft design.

The importance of icing determines the necessity to develop effective tools that are able to perform a prediction of the ice formation. The studies in this field started in late 1920s, but only with the World War II the first icing tunnels were built in response of the war effort [4]. Up until 1978, the studies were mainly experimental and focused on the icing effects on lift and drag coefficients, and in general the aerodynamic performances of the aircraft. In 1929, Carroll and McAvoy [5] recognized that the aerodynamic penalties of icing are more severe than an additional weight and their paper *"recommends avoidance of conditions under which this (ice formation) is most likely to occur"*. The modern study on aircraft-icing began in 1978, after a workshop proposed by NASA and FAA (Federal Aviation Administration) [6]: the computational fluid dynamics (CFD) began to be developed and be applied to the prediction of icing on the surfaces, and to compute the aerodynamic performances of airfoils with ice. The focus of icing research shifted in 1994, after the ATR-72 accident in Roselawn; indeed, the research changed *"its focus from a scientific exercise to one clearly focused on aircraft safety"* [4]. The report on the accident figured out that the issues on the control surfaces was caused by icing in particular condition; consequently, the research focused on different type of ice accretions, including the Supercooled Large Droplets (SLD), to identify the critical condition and design more effective Ice Protection Systems (IPS).

Flight tests, wind tunnel experiments and numerical simulations are complementary in the icing investigation; however, flight tests are complicated and particularly expensive since another aircraft or a specific system is needed to spray water droplet on tested craft; an example of flight test on a rotorcraft is shown in Fig. 1.1. Moreover, to perform a wind tunnel test, a special configuration is needed: the wind tunnel must operate at low controlled temperatures, resulting in higher operational cost than for classic aeronautical wind tunnel. For these reasons, the CFD simulations can be used during the design phase

to reduce the economic costs: it can be used to predict ice shapes, and the worsening of the aerodynamic and control performances of the aircraft surfaces. However, flight and wind tunnel tests cannot be totally replaced in the certification phase of a new aircraft.

Figure 1.1: AgustaWestland's AW189 icing trials of full icing protection system. [7]

The development of mathematical models defined to predict ice accretion stem from the work of Stefan [8], which was related to the formation of ice in the Artic Sea; the first model specifically defined for the aeronautical case was developed by Messinger in 1953 [9]. Nowadays there are several ice accretion codes capable of predicting different ice shapes for any types of ice in many geometries, and also three-dimensional cases. The huge database of experimental activity in different conditions, obtained in the first phase of icing research, is used to fine-tuning the models; moreover, the comparison between experimental and numerical data is used to define the reliability of the models.

However, numerical models and experimental tests are affected by uncertainty, which could put under question their reliability. For this reason, an uncertainty quantification study is needed to characterize and then reduce the source of uncertainties. It is possible to identify their main sources: uncertainty in the model inputs, such as the model parameters, the boundary conditions and forcing term; discrepancy between the model and the physics; uncertainty due to the algorithm, which is unavoidable in CFD; computational costs, due to the higher computational time and memory requirements needed for more precise models.
One of the main difficulties in UQ is to forward propagate the uncertainty. The aim is to evaluate the statistical moments of the numerical outputs propagated from uncertain inputs, namely, in this work, the uncertainties retrieved from the experimental setup. The stochastic analysis of the model allows to evaluate the reliability of the outputs and hence, the numerical model.

In this thesis, the uncertainty quantification will be performed on the computation of collection efficiency, which is the parameter that describes the fraction of water mass contained in the cloud collected at a certain location of the aircraft surfaces. The statistical moments are computed on the collection efficiency obtained on different airfoil and experimental conditions; furthermore, a comparison is performed between the conditions described in Appendix-C and Appendix-O of the FAA regulations. These appendices

define two different icing conditions and their respective regulations for the design of the aircraft: Appendix-C describes icing conditions and certification requirements for clouds containing droplets with Median Volume Diameter (MVD) of less than 40 μm and a lowest temperature of 233 K. At these temperatures only small droplets can exist in supercooled state and the assumption of spherical droplets can be assessed. After the ATR-42 accident, the Appendix-O was instead defined to consider different icing condition related with Supercooled Large Droplets (SLD), hence for higher temperature and for MVD larger than 40 μm; for these droplets the physics is more complicated because the particles are deformed by the aerodynamic shear forces, and they can splash or rebound when impacting the surfaces.

The uncertainty quantification on the collection efficiency can be assessed with different methods. In this work the Polynomial Chaos Expansion (PCE) will be employed to forward propagate the uncertainties of the input parameters, which are retrieved in the experimental setup from the literature. The aim of this method is to define a polynomial approximation of the results of the simulations, as a function of the random variables of interest. The objective is to compute the coefficients of the polynomial expansion: a good choice of the polynomial basis could, indeed, bring useful statistical information such as stochastic moments, probability density and sensitivity analysis; furthermore, this method could be less expensive in terms of computational cost than the Monte-Carlo and other sampling methods.
Even if this method is widely used in uncertainty quantification studies, at the time of writing, only a few research are published which employ it on ice accretion over aeronautical surfaces. [10–13], and even less UQ research consider the Appendix-O conditions [14].

1.1. Important parameter of ice accretion

Icing on aircraft surfaces happens when the flight is among clouds at a certain range of temperature, or when the aircraft encounters precipitations such as drizzle rain and snow. Under the freezing temperature of the water, the droplets should freeze and form ice; however, it is possible that the particles remain in the liquid state due to their relatively small size; this state of the particles is named Supercooled State. Here the particles can remain liquid at as far as 253 K, and down to 238 K if the droplets are very small; however, the latter case is less frequent [15]. In Supercooled state the particles can freeze spontaneously at a temperature below 233 K, or if a perturbation occurs on their unstable equilibrium, such as the impact on the aircraft surfaces.

The ice accretion can be divided in two different phases: the first one is related to the water particles impingement and its rate; the second one is related to the freezing rate of the water droplets collected on the surface. This work considers only the first phase of the ice accretion, which depends on different parameters: the local curvature of the surface; the velocity of the aircraft; the size of water particles contained in the clouds. The main parameters, considered in this work, will be described below.

Collection efficiency (β)

The collection efficiency β is the local value which describes the fraction of water mass which impacts, and it is collected at a given location on the surface. It is one of the most important parameters in icing since it is strictly related to the accretion rate; moreover, since it represents the water collected by the surface, it is useful to define the area where the ice accretion can occur. Given the trajectories of the particles, which in this work are computed using the Lagrangian approach (described in Sec 2.2), different schemes are available to compute β; however, all the methods link the initial cross-sectional area of the droplet stream tube to the area of impact on the surface. In two-dimensional geometries, the collection efficiency is approximated as the ratio between the total separation δy of the trajectories in the freestream, and the total separation δs between the trajectories at the impact on the surface (Fig. 1.2):

$$\beta = \frac{\delta y}{\delta s} \tag{1.1}$$

In three-dimensional geometries, instead, β can be defined as the area upstream dA_∞ over the surface dA_i enclosed by the same trajectories of the droplets (Fig 1.3):

$$\beta = \frac{dA_\infty}{dA_i} \tag{1.2}$$

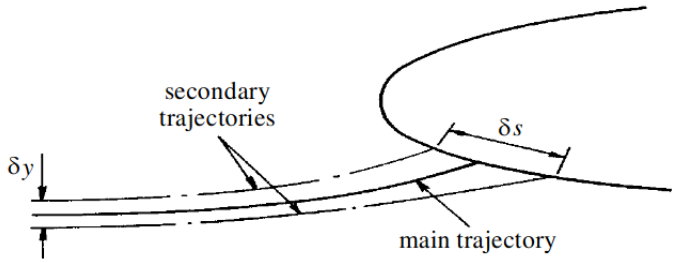

Figure 1.2: Collection efficiency computed for a two-dimensional geometry. Picture from [18].

The value of collection efficiency typical goes from 0 in the clean surface, to 0.8. It typically has a peak on the stagnation point of the surface, then decreases until it reaches 0. The point in the surface where β reaches 0 is defined as the impingement limit. High values of β are related to high values of icing rate.

Median Volume Diameter (MVD)

The Median Volume Diameter defines the median value of the probability distribution of the droplets diameter; this means that half the volume of the water is contained in droplets larger than the MVD value; the other half is contained in particles with a diameter below

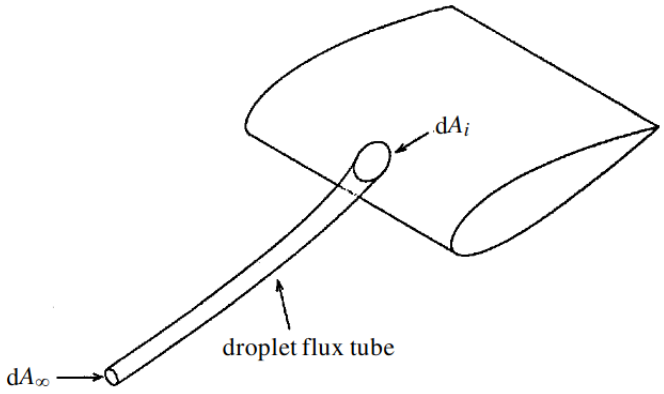

Figure 1.3: Collection efficiency computed for a three-dimensional geometry. Picture from [18].

the median value. MVD is typical between 15 and 40 μm, however, in this work, larger values will be considered. Droplets with diameter larger than 40 μm are called Supercooled Large Droplets.

As shown in Fig. 1.4, taken from the paper by Gent [18], the MVD directly affects β: the mass of water of a droplet is directly proportional the cube of its diameter, whereas the influence of the airflow on the droplet is directly proportional to the square of the diameter. Consequently, droplets with larger diameter have the tendency to follow straighter trajectory because they are less affected by the local aerodynamic force; on the other hand, the small particles have smaller mass and tend to follow the streamlines, hence the latter could not impact the surfaces resulting in a lower collection efficiency. In Fig. 1.4, it is also possible to highlight that for higher MVD, the area where the droplets impinge is larger, hence the impingement limits are moved further aft.

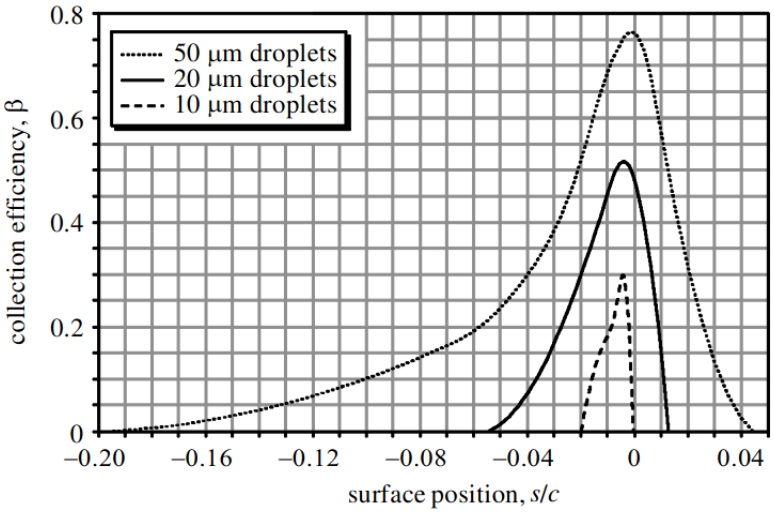

Figure 1.4: Effect of MVD on the collection efficiency. [18]

Liquid Water Content (LWC)

The LWC expresses the mass of water per cubic metre of air. Generally, it is expressed as g/m^3. The term Liquid indicates the supercooled nature of the droplets and acts to distinguish the state of the cloud from the ice crystal alternative. In general, a larger value of LWC implies a larger mass of water collected, hence a larger accumulation of ice. However, this is not strictly correct since the collection efficiency is equally important. If a large mass of water is contained in particles small enough to have no capability to impact on the surface, the resulting ice accretion will be small. Typically, LWC values are between $0.2\,g/m^3$ and $1.5\,g/m^3$, depending on the type of cloud.

Freestream velocity (u_∞)

The airspeed is not an icing condition itself, but it influences the water collected. At a given time, the higher velocity of the aircraft, the larger is the intercepted volume of air, and hence, the larger the mass of water that impacts on the surfaces. It is therefore the product of the collection efficiency, the LWC and the speed of the aircraft or the rotor which determines the mass of water that will impact the surface, and hence the amount of accretion.

1.2. Scope and structure of the thesis

The design of new aircraft and ice protection system must follow strict regulations and nowadays the flight tests are still used to assess the required certification. However, they are very expensive and in order to reduce the operational costs, the numerical prediction of ice accretion is a useful tool in the design phase of a new aircraft.

However, the reliability of numerical simulations and the computational models are questioned by the uncertainties. Their derive from the approximation in the numerical models as well as the uncertainty in the experimental setup. This work aims to forward propagate these uncertainties throughout the numerical simulations using PCE to compute the statistical moments. Moreover, the objective is to perform a sensitivity analysis on the different input parameters to define their influence on the uncertainty. The analysis is performed on two different airfoil, namely a MS(1)-317 and a NACA-23012, and for different MVD considering also the SLD regime. The sensitivity analysis is performed computing the Sobol indices. To assess the accuracy of numerical predictions over real data, the predicted collection efficiency is compared with data of wind tunnel tests carried out in NASA Glenn Icing Research Tunnel (IRT). In particular, the focus is on particles lying in SLD regime: these droplets, due to their bigger size, tend to deform under the influence of aerodynamic shear forces and they could splash or rebound when impacting the aircraft surfaces.

The present work is organised as follows. In Chapter 2 the governing equations to compute the particle trajectory are presented both for small particles and SLD regime; moreover, the LEWICE splash model, used to compute β, is described. In Chapter 3, the theory of

Polynomial Chaos Expansion is presented; furthermore, the algorithm used to assess the uncertainty quantification is also described in detail. Chapter 4 deals with the presentation of the results and their comparison with the experimental data from the literature; furthermore, a stochastic analysis is also performed investigating the statistical moments and the Sobol indices obtained for each case. Eventually, Chapter 5 provides conclusions and recommendations for future developments.

2 | Lagrangian particle tracking

The main objective of this chapter is to explain how the collection efficiency β will be computed on the surface of the body, both in the theory and the computational setup. For the latter a particle tracking code is needed and this work has exploited PoliDrop, an in-house software. The chapter will briefly describe the algorithm, the models used and eventually the results of the simulations in comparison with the experimental data extracted from the literature.

2.1. Introduction

First of all, it is necessary to compute the characteristics of the flow field with a CFD solver. SU2 has been chosen, which is *"an open-source collection of software tools written in C++ and Python for the analysis of partial differential equations (PDEs) and PDE-constrained optimization problems on unstructured meshes with state-of-the-art numerical methods"* (see [16] for more details). It includes, among others, tools to compute compressible and incompressible Euler equations, Navier-Stokes equations and also RANS solver. In particular, it provides a grid-based solution in which the velocity is known in certain discrete points by interpolating the velocities of the surrounding points. The models and the solvers implemented consequuently allow the operator to choose the most suitable solver for the specific case studied. The ones selected for this work are described in Sec. 2.5.

The purpose of PoliDrop is to track down the clouds particles and their impact on the surface and then to compute the collection efficiency.
Regarding the computation of the particles' trajectory, there exist two different approaches: the Eulerian approach and the Lagrangian approach. The Eulerian approach is based on a set of partial differential equation representing the continuity and the momentum equations so that the volume fraction is computed directly on the nodes of the grid ensemble with the flow variables and it is not tracked the trajectory of each particle [17]. This approach is particularly useful in complex three-dimensional geometry or flows and it is gaining relevance in the last few years. On the other hand, the Lagrangian approach tracks the trajectory of each particle from the starting point to the impact or to the end of the simulation's time and it's commonly used for simpler problems due to the larger computational costs which increase with the number of drops.

2.2. Governing equations

In this work the Lagrangian approach will be used for the computation of the particle solution. The code integrates in time the equations for droplets trajectory. It is necessary to set some assumptions to derive the equation used [18]:

- The droplets are spherical and they do not deform.
- There is no collision or coalescence of droplets.
- Turbulence effects may be neglected except those affecting the mean flow field.
- The only forces acting on the droplet are due to aerodynamic drag and buoyancy. The effects of gravity are not taken into account, as they are considered negligible with respect to aerodynamic forces.
- The water droplet concentration is sufficiently small for the droplets to have a negligible effect on the aerodynamic flow and, therefore, the airflow and water droplets may be treated as independent systems.

Based on these assumptions the equations for the trajectory are derived from the momentum equation:

$$m_p \frac{d\mathbf{u_p}}{dt} = \mathbf{F_a} \tag{2.1}$$

where m_p is the mass of the particle computed from the density and the volume of the particle and $\mathbf{F_a}$ are the aerodynamic forces effecting on the particle:

$$m_p = \rho_p \frac{4}{3}\pi \left(\frac{d_p}{2}\right)^2 \tag{2.2}$$

$$\mathbf{F_a} = \frac{1}{2}\rho_f \left(\mathbf{u_f} - \mathbf{u_p}\right) C_D \pi \left(\frac{d_p}{2}\right)^2 \tag{2.3}$$

Where ρ_f and $\mathbf{u_f}$ is respectively the density and the velocity of the flow and C_D is the drag coefficient which is an important point of the numerical model and it will be explained in Sec. 2.3.
Substituting eq. 2.2 and eq. 2.3 in the momentum equation and defining the relative Reynolds number of the particle:

$$Re_p = \frac{\rho_f d_p \left(\mathbf{u_f} - \mathbf{u_p}\right)}{\mu_f} \tag{2.4}$$

The system 2.5 is obtained where the quantities with the subscript p are referred to the particle and f to the flow:

$$\begin{cases} \dfrac{d\mathbf{u_p}}{dt} &= \dfrac{3}{4}\dfrac{C_D Re_p \mu_f}{\rho_p d_p^2}\left(\mathbf{u_f} - \mathbf{u_p}\right) \\ \dfrac{d\mathbf{x_p}}{dt} &= \mathbf{u_p} \end{cases} \tag{2.5}$$

The system describes the trajectory of the particle, where the first equation is its acceleration and the second its velocity. The trajectory is obtained by integrating in time the system 2.5. PoliDrop adopts the forward Euler method to solve the system. For the sake of this work, the method is only briefly described:

1. retrieve the flow variables at the nodes of the owner cell because the aerodynamic field was computed on a node-centered Finite Volume (FV) discretization as will be explained in the following;
2. interpolate the aerodynamic solution at the particle position;
3. solve the system 2.5 and compute the new position and velocity;
4. find the new owner cell and compute the boundary intersection if needed. The new owner is found using a known vicinity search algorithm that finds the new owner by computing the intersections between the particle trajectory and the faces of the crossed elements (Fig. 2.1).

The process is iterated until one of the following situation is obtained: the final integration is reached, the droplet has left the domain (this case is better to be avoided), or the particle has impinged on the surface. In conclusion, the collection efficiency in the algorithm is computed as the ratio between droplet panel density and cloud density. The droplet panel density is defined as the number of parcels impinging on the panel divided by its area. The cloud density is computed as the total number of droplets in the cloud, divided by the volume of the cloud:

$$\beta = \frac{collected\ parcels/panel\ area}{total\ parcels/cloud\ volume} \tag{2.6}$$

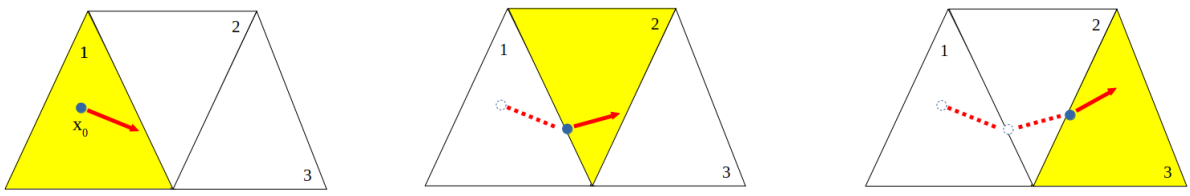

(a) (b) (c)

Figure 2.1: Scheme of the PoliDrop algorithm computation

2.3. Cd-Re model

In Eq. 2.3, C_D is the drag coefficient of the particle. The particles are assumed as spherical, therefore C_D is approximated as the drag coefficient of a sphere. There are several models to describe it as a function of the particle Reynold number. The simplest one is the Stokes model which works well for $Re < 10^0$. Increasing Re the model differs from the experimental data and corrections to this model are introduced. Some models are presented (eq. 2.7 - 2.11) while others can be found in [18] and [19].

$$C_{D_{Stokes}} = \frac{24}{Re} \tag{2.7}$$

$$C_{D_{Gent}} = \frac{24}{Re}\left(1 + 0.197Re^{0.63} + 2.64 \times 10^{-4}Re^{1.38}\right) \tag{2.8}$$

$$C_{D_{Schiller\ Naumann}} = max\left(\frac{24}{Re}\left(1 + 0.15Re^{0.687}\right), 0.44\right) \tag{2.9}$$

$$C_{D_{Morris}} = \frac{24}{Re} + 2.6\frac{\frac{Re}{5}}{1+\left(\frac{Re}{5}\right)^{1.52}} + 0.411\frac{\left(\frac{Re}{263000}\right)^{-7.94}}{1+\left(\frac{Re}{263000}\right)^{-8}} + \frac{Re^{0.8}}{461000} \tag{2.10}$$

$$C_{D_{Shankar\ Subramanian}} = 0.19 - \frac{8 \times 10^4}{Re} \tag{2.11}$$

The models can be linked to define a better approximation for a large scale of Reynolds number:

$$C_{D_{MSS}} = \begin{cases} C_{D_{Morris}} & Re < 10^6 \\ C_{D_{Shankar\ Subramanian}} + \delta & Re > 10^6 \end{cases} \tag{2.12}$$

where $\delta = 0.0315$ is a correction factor needed to link the two curves. As shown in fig. 2.2, this is the best model to fit the experimental data

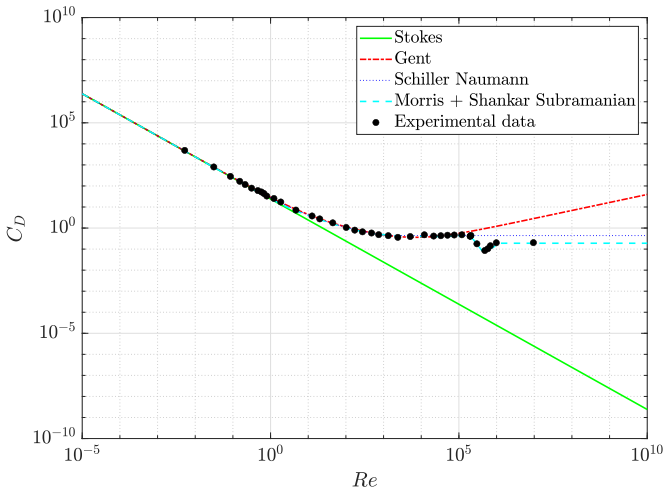

Figure 2.2: Representation of the different C_D model of the sphere as a function of Re and the experimental data retrieved in [19]

2.4. Splash model

As mentioned before, this work considers also some cases where MVD is larger than 40 μm and they are defined as Supercooled Large Droplet (SLD). These droplets can violate the assumption of sphericity made for the previous case (see Sec. 2.2). Large droplets can bring different icing condition from the icing described in Appendix-C of FAA (Federal Aviation Administration) regulation. The regulation requirements used to consider only clouds with a maximum droplet diameter $d_{max} < 100\mu m$ [20], but in 1990's the regulations was expanded to include SLD in order to increase the level of safety. The new rule was introduced after the accident occured to an ATR-72 aircraft in 1994 in Roselawn, Indiana. The report on the accident compiled by the National Transportation Safety Board (NTSB) reported that *"the probable causes of this accident were the loss of control, attributed to a sudden and unexpected aileron hinge moment reversal that occurred after a ridge of ice accreted beyond the deice boot"* due to a prolonged operation in freezing drizzle environment beyond the certification envelope. After this report, the Appendix-O to the regulation was written to define the different icing condition and the new certification requirements (for a more depth analysis see [21]).

The reason behind the different behaviour of larger droplet lies in the fact that the particles can deform due to the aerodynamic and shear forces, leading to a grater aerodynamic drag. They can lead to a phenomenon called run-back ice, this is crucial, because ice accretion could extend on the entire surface of the wing and not only on the leading edge, compromising the ice protection systems (IPS). This is the problem that occured on the ATR-72 in Roselawn. The phenomenon is caused, in particular, by the possibility of larger droplets to bounce or to splash: only a partial fraction of the particle impinge the leading edge, while the other fraction is reintroduced in the flow field, making a new impingement in the back of the wing possible. This chance of splashing and rebounding is the reason why modelling the SLD cases is more complicated than the other cases, and it is necessary to modify not only the ice accretion model, but also the particle tracking model as described in the next section.

2.4.1. Extended $C_D - Re$ model

The three main forces acting on the particles which determine their deformation and breakup are the dynamic pressure and the viscous forces, which enhance the deformation, and the surface tension σ, which counteracts the deformation. A new dimensionless number is therefore defined to determine the flow condition: the Weber number, which is the ration between the inertial forces and the surface tension:

$$We = \frac{\rho_p \mathbf{u_p}^2 d_p}{\sigma} \tag{2.13}$$

in particular, what is needed is the breakup Weber number

$$We = \frac{\rho_p \left(\mathbf{u_f} - \mathbf{u_p}\right)^2 d_p}{\sigma} \tag{2.14}$$

This parameter governs the deformation of the droplet. It goes from a sphere to a final shape similar to a disk, passing for an oblate spheroid as shown in Fig. 2.3, from the article by Kékesi [22].

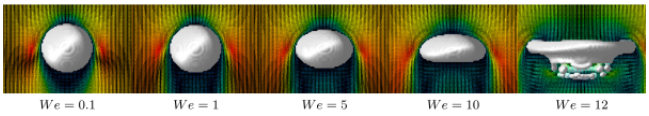

Figure 2.3: Deformation increasing the Weber number [22]

It is possible to relate the shape of the particle and the drag coefficient by defining f, the eccentricity function of the particle. f is defined as the difference between the equatorial and polar axis divided by polar axis as defined in 2.15:

$$f = \frac{c-a}{c} = 1 - \frac{a}{c} \tag{2.15}$$

c is the polar axis and a in the equatorial axis. When c tends to a, f tends to 0 so the particle tends to be a sphere. If f is equal to 1, the particle tends to be a flat disk.
According to Honsek and Habashi [23], it is possible to define f as a function of the breakup Weber number

$$f = 1 - \left(1 + 0.07\sqrt{We_b}\right)^{-6} \tag{2.16}$$

and consecutively the drag coefficient could be written as a function of f

$$C_D = \begin{cases} (1-f)\, C_{D_{sphere}} + f C_{D_{disk}} & We_b < 12 \\ C_{D_{disk}} & We_b > 12 \end{cases} \tag{2.17}$$

before reaching the limit breakup Weber number, which is equal to 12, the drag coefficient is thus a weighted mean between the C_D of the sphere and the disk; then the droplet breaks up and it is modelled as the drag coefficient of the disk. For the sphere, the model used is the one by Morris and Shankar Subramanian as defined in Eq. 2.12; for the disk, a model defined by Clift [18] is considered:

$$C_{D_{disk}} = \begin{cases} \dfrac{64}{\pi Re}\left(1 + \dfrac{Re}{2\pi}\right) & Re \leq 0.01 \\ \dfrac{64}{\pi Re}\left(1 + 10^x\right) & 0.01 \leq Re \leq 1.5 \\ \dfrac{64}{\pi Re}\left(1 + 0.138 Re^{0.792}\right) & 1.5 \leq Re \leq 133 \\ 1.17 & Re \geq 133 \end{cases} \tag{2.18}$$

where Re is Re_p of Eq. 2.4 and $x = -0.883 + 0.906\,(log_{10}Re) - 0.025\,(log_{10}Re)^2$. As shown in Fig. 2.17 the drag coefficients are almost the same at low Reynolds number and differs when Re increases.

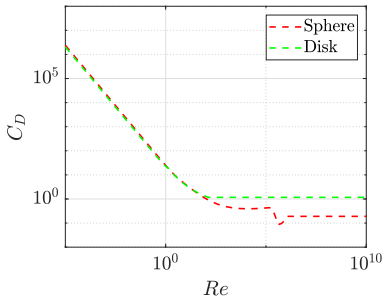

Figure 2.4: $C_D - Re$ curves for sphere and disk

2.4.2. LEWICE Splashing Model

In order to compute the collection efficiency and to take into account the possibility of the particle to splash and bounce, the model used is the LEWICE splashing model [24] developed by NASA. This is a semi-empirical model where the two possible effects of the drops impinging the surface are combined into a single correlation, determined by matching the β results of the experimental database on ice shapes and collection efficiencies generated in the NASA Glenn Icing Research Tunnel [25–27]. Before describing the model, the Ohnesorge number needs to be define: this is the ratio between viscous forces and the product between the inertial forces and surface tension:

$$Oh = \frac{\sqrt{We}}{Re} = \frac{\mu_p}{\sqrt{\sigma \rho_p d_p}} \tag{2.19}$$

According by the studies of Mundo, Sommerfeld and Tropea [28–30], splashing occurs when $K = Oh\, Re^{1.25} > 57.7$.

In LEWICE splashing model the parameter use to define if the splash occur is K_L:

$$K_L = \frac{0.859\sqrt{Oh_w Re_w^{0.125}}\left(\frac{\rho_w}{LWC}\right)^{1.25}}{(\sin\alpha_{imp})^{1.25}} \tag{2.20}$$

Where the subscript w stand for "water" and α_{imp} is the impingement angle of the droplets on the surface.
If $K_L > 200$, then the fraction of mass loss is determined by:

$$\frac{m_{loss}}{m_{imp}} = 0.7\ (1 - \sin\alpha_{imp})\ (1 - \exp\left(-0.0092026\ (K_L - 200)\right)) \tag{2.21}$$

It is interesting to note that if α_{imp} is equal to 90°, so that the droplets are impinging perpendicular to the surfaces, there is no splashing.

2.5. Comparison with experimental data

In this last section of the chapter, the results on the collection efficiency obtained with PoliDrop are compared with the experimental data from a NASA report [33]. The simulations are run both considering splashing and rebounding with the LEWICE splashing model, and also not using it, in order to show the different solutions obtained. The airfoil used for the tests is a MS(1)-317 shown in Fig. 2.5. It was designed in mid 1970's for general aviation aircraft [31]. The two-dimensional model of the airfoil used for the test is made of fiberglass skin and has a chord of 0.914 m.

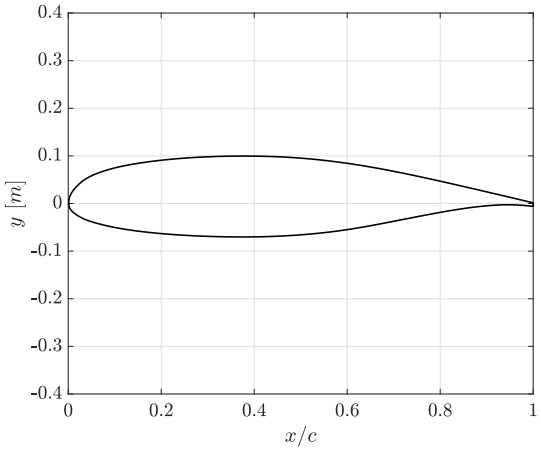

Figure 2.5: MS(1)-317 airfoil used for simulations

Experimental tests were conducted at the NASA Glenn Icing Research Tunnel (IRT): a refrigerated closed-looped tunnel that can have a controlled temperature and pressure. The closed test section can reach a range of controlled temperature from $244K$ to $273K$. The droplets are generated by a spraying system capable of recreating clouds with LWC of $0.3 - 3\,g/m^3$ and MVD of range between $14 - 40\,\mu m$ but also from 70 to $270\,\mu$m for a limited range of clouds. Further details concerning the IRT facility are provided in [34]. The tests are performed at a velocity of 80 m/s and an angle of attack of 8°. The static pressure is set to 94 806 Pa corresponding to an altitude of 598 m. The collection efficiency is determined by a dye-tracer method, which consists in a known concentration of blue dye put in distilled water and sprayed in the air stream through a specifically designed system of 16 nozzles. The airfoil model is covered in thin strips of blotter paper in the areas of interest and exposed to the spray for a certain time. Using a spectroscopy reflectance technique, which quantitatively measures the color and density of the light reflected by the surface, it is possible to determine the dye mass per unit area. Then, the collection efficiency is retrieved by converting the dye color density distribution on each strip in to the water impingement density, by using the developed calibration curves.

As for what concerns the computational setup, the numerical simulations are computed on a hybrid mesh of 42116 elements. Near the surface quadrilateral elements are used in order to better catch the boundary layer. In the free stream, triangular elements are used. Before computing the simulations using PoliDrop, a study of grid convergence has

been carried out. In order to take into account the errors due to the closed test section of IRT a study to retrieve the angle of attack has been performed to best reproduce the experimental condition. To achieve that, this work compares the curve of the pressure coefficient along the airfoil, resulting from the SU2 simulations at different angles of attack, and the experimental data from [33] as shown in Fig 2.6. In accordance to the experimental data, the AoA chosen for the PoliDrop simulations is 6.5^o

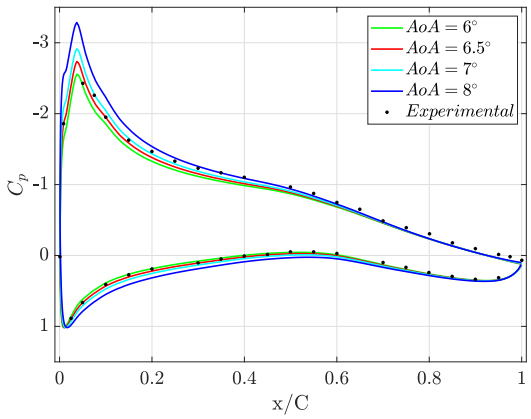

Figure 2.6: $C_p - x$ curves for different angle of attack compared with the experimental data from [33]

As mentioned before, the CFD solver used in this work is SU2 and the flow field is computed solving the Reynolds Averaged Navier-Stokes equations (RANS) using the Shear-Stress Transport model (SST) proposed by Menter [32]. This is a two-equation model which combines the $k - \epsilon$ and the $k - \omega$ models where k is the turbulent kinetic energy, ϵ is the dissipation ratio and ω is the characteristic frequency of the eddies defined as $\epsilon \,/\, k$. It combines the equation through a scaling factor, which near the surface tends to 0 so that the equation is identical to $k - \omega$ model; in the outer region instead, the model tends to $k - \epsilon$. SST model take the computational advantages of the latter, avoiding its singularity at the wall. This method is nowadays largely used in the industrial sector, especially in turbomachinery.
Once the flow is computed, the collection efficiency β is retrieved with PoliDrop, setting the initial position of the cloud. In the case where the splash and rebound of particles are not considered, a branch of the software named CloudAdaption is used. For every iteration it performs an adaptation of the cloud for better computing the collection efficiency. When considering the splash and rebound a convergence study, varying the number of parcels in y-direction, is needed. It is important to consider that, studying too few particles could provide a poor solution, while taking into account too many of them would increase the computational cost. For both cases it is important to set the right time of the simulation and the delta time of the integration in order to obtain the impingement of each particle over the entire surface, but avoiding their exit from the domain.
Collection efficiency is presented as a function of the curvilinear abscissa where 0 is the leading edge, the positive x is the upper surface of the airfoil and the negative x is the lower one. The curve presents a skewness due to the profile and the angle of attack: this

implies a greater impingement on the top of the airfoil.

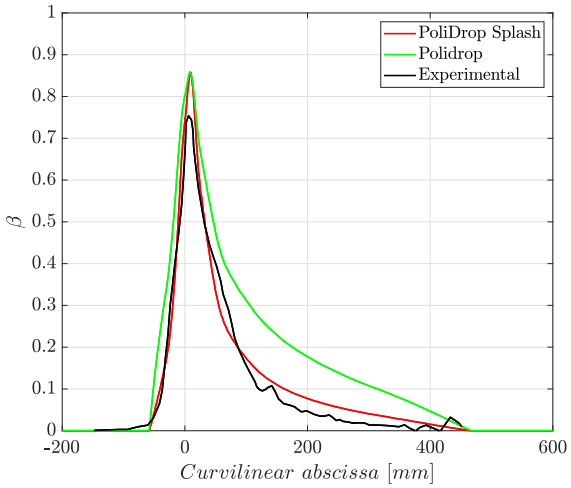

Figure 2.7: Comparison between PoliDrop simulations and experimental data from [33]

The simulations present a good fit with experimental data, especially using the splash model, as expected due to MVD= $92\mu m$. Only the peak is overestimated; this is where there is the peak of the variance on the results as presented in Chapter 4.

3 | Uncertainty quantification

As shown in Fig. 2.7, the nominal condition does not perfectly fit the experimental data and this is not only due to the approximation in the numerical model. The main reason can be retrieved in the uncertainty of experimental settings, which implies that a stochastic computation must be applied in order to forward propagate these uncertainties. A commonly used method to forward propagate the uncertainty is the Monte Carlo Sampling (MCS) method or one of its variants. It consists in computing independent realizations of random inputs, based on their prescribed probability distribution. For each realization the input values are fixed so that the problem becomes deterministic. The statistical information is then extracted from these realizations. This method is simple, but has a significant drawback, as large number of realizations is needed in order to obtain accurate results; many realizations lead to an excessive computational cost, especially in systems which are computationally expensive in their deterministic settings. A method which goes beyond this limit is the Polynomial Chaos Expansion (PCE) method and it will be applied in this work to execute the statistical analysis. This method is nowadays widely used in uncertainty quantification studies, but few studies are implementing it in aeronautical case, and even less in Appendix-O conditions.

The PC expansion is a probabilistic method consisting in the projection of the model output on a basis of orthogonal stochastic polynomials in random inputs. The projection provides a compact and convenient representation of the model output variability with regards to the inputs.
The idea is to build a polynomial approximation of the results of the simulations as a function of the random variables of interest, with the aim is to compute the coefficients of the polynomial expansion. A good choice of the polynomial basis could bring useful statistical information such as stochastic moments, probability density and sensitivity analysis; furthermore, this method could be less expensive in terms of computational cost than MCS and other sampling methods.
With PCE, it is possible to write a surrogate of the CFD model, which links the Quantities of Interest (QoIs), i.e. the output of the model, to the random variables of input.

3.1. Polynomial Chaos Expansion

Polynomial Chaos expansion was introduced by Wiener in 1938 [35] and it well approximates any random variable by a series of polynomials in centered normalized Gaussian variables. Considering a set of infite independent random variables $\xi \doteq [\xi_1, \xi_2, ...]$, in which each variable has a known normalized gaussian probability density $p(\xi)$. Consid-

ering a function $f(\xi)$, which is a random variable itself due to its dependency on random parameters, it is possible to write f as a series of polynomials multiplied by appropriate coefficients:

$$f(\xi) = \sum_{k=0}^{\infty} c_k \Psi_k(\xi) \tag{3.1}$$

where c_k are deterministic coefficients, namely the PC coefficients of the expansion, and k indicates the polynomial order. For practical reasons, the upper index of the series has to be truncated at an arbitrary value P; a finite number d of Gaussian variables are used for the same reason. The latter is not a limitation since the physical problem has a finite number of random inputs as presented in Sec. 3.2.
Ψ are random polynomial basis chosen to be orthogonal in the L_2 space following the relation:

$$\langle \Psi_i(\xi), \Psi_j(\xi) \rangle = \int \Psi_i(\xi) \Psi_j(\xi) p(\xi) d\xi = \langle \Psi_i(\xi)^2 \rangle \delta_{ij} \tag{3.2}$$

These polynomials are multi-variate Hermite polynomials which represent the best choice for these cases. One of their definition in one dimension is:

$$He_i(x) = (-1)^i e^{\frac{x^2}{2}} \frac{d^i}{dx_i} \left(-e^{\frac{x^2}{2}} \right) \tag{3.3}$$

where i is the order of the polynomial.
The convergence of 3.1 is ensured in a L_2-sense, as shown by Cameron and Martin in [36]. Eventually, the finite dimensional and finite PC order of expansion lead to:

$$f(\xi) = \sum_{k=0}^{P} c_k \Psi_k(\xi) \tag{3.4}$$

The basis dimension is retrieved from d and p:

$$P + 1 = \frac{(p+d)!}{p!d!} \tag{3.5}$$

For example: in this work the independent variables are 5 and the approximation is a third order polynomials; the PC expansion will consequently have 56 terms.
The PC expansion proposed by Wiener can be applied to measures which have Gaussian probability distribution, but it can be also generalized for non-Guassian probability densities, as presented by Xiu and Karniadakis [37] using the Wiener-Askey scheme presented in Table 3.1.

Once the PCE coefficients are computed, the statistical moments and sensitivity analysis can be straightforwardly derived by manipulating the coefficients. For example the expected value of the output $\overline{y}$, which is related to one of the quantities of interest (QoI) $y = f(\xi)$, is:

Distribution	Orthogonal polynomial	Support
Gaussian	Hermite	$(-\infty, +\infty)$
Uniform	Legendre	$[-1, 1]$
Exponential	Laguerre	$[0, +\infty)$
Poisson	Charlier	$\{0, 1, 2, ...\}$
Binomial	Krawtchouk	$\{0, 1, 2, ..., N\}$

Table 3.1: Examples of different variable distribution and orthogonal polynomial family

$$\begin{aligned}
\overline{y} = E[y] &\approx E\left[\sum_{k=0}^{P} c_k \Psi_k(\xi)\right] \\
&= \int_{\mathbb{R}^P} \left(\sum_{k=0}^{P} c_k \Psi_k(\xi)\right) p(\xi)\, d\xi \\
&= \sum_{k=0}^{P} c_k \int_{\mathbb{R}^P} 1 \cdot \Psi_k(\xi)\, p(\xi)\, d\xi \\
&= \sum_{k=0}^{P} c_k \langle \Psi_0, \Psi_k \rangle \\
&= c_0 \langle \Psi_0, \Psi_0 \rangle = c_0
\end{aligned} \tag{3.6}$$

The expected value is therefore the first coefficient of the polynomial expansion and it is obtained using the property of the expected value and the orthogonality of the polynomials.
Using the same approach it is possible to derive the variance of the system:

$$\sigma^2 = E\left[(y - \overline{y})^2\right] \approx \sum_{k=1}^{P} c_k^2 \tag{3.7}$$

Another important advantage of using the PCE is that it allows to directly derive the *Sobol indices* [38]; the indices can then be applied in a global sensitivity analysis; in order to study which parameters influence more the uncertainty of the output. As presented by Crestaux and Le Maître [39], the Sobol indices, and even more the Sobol's decomposition and the ANalysis Of VAriance (ANOVA) decomposition, can be directly deduced from the PCE of the model output. In the next paragraph the main passages of the theory are presented; more in depth, demonstrations and details can be retrieved in [39]. Starting from the Sobol decomposition:

$$f(\xi) = \sum_{u \subseteq (1,2,...,d)} f_u(\xi_u) \tag{3.8}$$

Where u is a set of integers $\xi_u = (\xi_{u_1}, ..., \xi u_s)$, with $s = card(u) = |u|$.

Defining D as the variance of the output $y = f(\xi)$ and D_u as the conditional variances of the function f_u of the Sobol decomposition:

$$D = \int_{\Omega^d} f^2(\xi)\, p(\xi)\, d(\xi) - f_0^2 \tag{3.9}$$

$$D_u = \int_{\Omega^{|u|}} f_u^2(\xi_u)\, p(\xi_u)\, d(\xi_u) \tag{3.10}$$

The Sobol indices are defined by:

$$S_u = \frac{D_u}{D} \tag{3.11}$$

so that:

$$\sum_{\substack{u \subseteq (1,2,\ldots,d) \\ u \neq \emptyset}} S_u = 1 \tag{3.12}$$

In PCE it is possible to define a simple expression for the variance and the covariances:

$$\begin{aligned} \hat{D} &\approx \sum_{k=1}^{P} c_k^2 (\Psi_k, \Psi_k) \\ \hat{D_u} &\approx \sum_{k=K_u}^{P} c_k^2 (\Psi_k, \Psi_k) \end{aligned} \tag{3.13}$$

where K_u are a set of indices that only depend on the PC basis and not on the function f:

$$\mathbf{K}_u = \{k \in \{1, \ldots, P\} \,|\Psi_k(\xi) = \prod_{i=1}^{\|u\|} \phi_{\alpha_i^k}(\xi_{u_i}), \alpha_i^k > 0\} \tag{3.14}$$

Where ϕ_k represent the one-dimensional polynomial which composes the orthogonal basis. The Sobol indices is therefore computed as:

$$S_u \approx \hat{S}_u = \frac{\hat{D}_u}{\hat{D}} \tag{3.15}$$

Each of the Sobol sensitivity indices measures the sensitivity of the variance of y with respect to the interaction between the variables ξ_u. Since there are $2^d - 1$ Sobol indices, they quickly increase when the variables increase.

The orthogonal basis of the expansion are known and they are chosen in accordance with the probability densities; the only unknowns are the coefficients of the expansion. When c_k are computed, the expansion of the output y can be retrieved and it is possible to make a complete characterization of the uncertainty and, therefore, perform a sensitivity analysis.
In this work, y is the result of a numerical simulation, i.e. the output of mathematical

model. Traditionally, for this cases there are two classes of methods to compute the PCE coefficients for this case: the intrusive methods and the non-intrusive ones. In the intrusive method the objective is to define a weak solution by means of a Galerkin projection of the model equations on the PC basis. This method is more complex with respect to the non-intrusive one because in CFD applications it requires access to the source code of the computational solver. On the contrary, the non-intrusive methods require a finite set of deterministic realizations of the numerical code where the input can be sampled with different strategies. For example, in this work a Latin-Hypercube Sampling (LHS) method is employed as will be explain in Sec. 3.3.3.
Among the non-intrusive methods, there are several methods to compute the PC coefficients, such as the Non-Intrusive Spectral Projection (NISP) or the Least Square (LS) approach; the latter is applied in this work and it consists in retrieving the PC coefficients that minimize the approximation error, so that the square of the residual:

$$\mathbf{c} = \min_{c \in \mathbb{R}^P} \sum_{i=0}^{d} \left\| f\left(\xi^{(i)}\right) - \sum_{k=0}^{P} c_k \Psi_k\left(\xi^{(i)}\right) \right\|^2 \tag{3.16}$$

Where the function $f\left(\xi^{(i)}\right)$ is unknown, except at i data points. The matrix Z is defined as:

$$Z = \begin{pmatrix} \Psi_0\left(\xi^{(0)}\right) & \Psi_1\left(\xi^{(0)}\right) & \cdots & \Psi_P\left(\xi^{(0)}\right) \\ \Psi_0\left(\xi^{(1)}\right) & \Psi_1\left(\xi^{(1)}\right) & \cdots & \Psi_P\left(\xi^{(1)}\right) \\ \vdots & \vdots & \ddots & \vdots \\ \Psi_0\left(\xi^{(d)}\right) & \Psi_1\left(\xi^{(d)}\right) & \cdots & \Psi_P\left(\xi^{(d)}\right) \end{pmatrix} \tag{3.17}$$

3.2. Uncertain parameters in icing simulations

The phenomenon of the collection of water on the aircraft depends on a set of different uncertain parameters: the freestream pressure and temperature, which are related to the aerodynamic environment; the Median Value Diameter that characterizes the cloud; and the flying condition with the Mach number and the Angle of Attack. These inputs have several uncertainties due to the experimental setup; in this work, they are assumed as uniformly distributed within an interval centered on their nominal values. The aim is to recreate the conditions present in the wind tunnel.
The nominal test conditions and the uncertainty bound for the MS(1)-317 airfoil are presented in Table 3.2 and they are imposed in accordance with the data reported in cited work [33].

Mach	Pressure [Pa]	Temperature [K]	MVD [μm/s]	AoA [deg]
0.24 ± 0.03	94540 ± 134	277 ± 0.5	92 ± 18.4	6.5 ± 0.2

Table 3.2: Nominal test conditions and uncertainty bounds for MS(1)-317 case

For the Median Value Diameter the uncertainty is $\pm 12\%$ of the nominal value for droplets with MVD smaller and around $SI 50 \mu m/s$, and an uncertainty of $\pm 20\%$ for larger parti-

cles. The uncertainties are in accordance with the recent experimental setup of the IRT mist generator [40].
For the case study of NACA-23012 airfoil, the MVDs considered are 20 μm/s, 52 μm/s, 111 μm/s, 154 μm/s and 236 μm/s, and their uncertainties coincide with the ones mentioned above. The other parameters and their uncertainties are the same for each of the five MVD cases and are presented in Table 3.3.

Mach	Pressure [Pa]	Temperature [K]	AoA [*deg*]
0.23 ± 0.03	94860 ± 134	289.9 ± 0.5	2.5 ± 0.2

Table 3.3: Nominal test conditions and uncertainty bounds for NACA-23012 cases

Every parameter of each case is uniformly distributed, but, as explained in Sec. 3.1, this is not a limitation due to the generalization of PCE by Xiu [37].

3.3. Algorithm

This section presents the algorithm used for every case considered. The results for each specific will be presented in Chapter 4.

3.3.1. Grid convergence

The first step of the work is to perform a convergence study on the mesh. The dual aim is to ensure the correct computation of the flow and to avoid using mesh with too many elements which would lead to an excessive computational burden. The meshes taken into account are hybrid and compiled by the software UhMesh, which is a hybrid mesh generation code for high-Reynolds flows [41]. The mesh is structured near the surface, so that rectangular elements are employed to better compute the boundary layer; in the outer region the mesh is unstructured with triangular elements in which their lengths increase when the distance from the airfoil increases.
To make the grid convergence, several CFD simulations on SU2 are run with the same inputs over meshes with increasing number of elements. The aerodynamic field around the airfoil is computed using the SU2 RANS solver where the RANS equations are discretized using a finite volume method with a standard edge-based structure. Convective fluxes are discretized using a limited second order MUSCL scheme with an Approximate Riemann Solver (ARS) of Roe type. The Venkatakrishnan flux limiter is employed. Viscous fluxes are discretized using a standard average of gradients approach. Source terms are approximated at each node using a piecewise-constant reconstruction within each control volume. Gradients are obtained using a weighted least-squares approach. A time-marching approach is used to drive the RANS system to a steady solution using an implicit Euler scheme. The convergence of the simulation is monitored by checking the root mean square of the density equation residual and it is stopped when the residual is eight order smaller than the first iteration.
The input parameters of the simulations are set as reported in [33] and they are the nominal values of Table 3.3 for the NACA-23012 and Table 3.2 for the MS-317 case, with

the exception of the AoA which is equal to 8^o in accordance with the NASA report (the reason of this difference will be explained in Sec. 3.3.2).

The convergence of the mesh is then checked by the lift coefficient C_L. After a certain number of elements, the value of C_L slightly changes and the convergence is obtained.

3.3.2. Replicate test condition

The next step is to retrieve the nominal test conditions of the wind tunnel, so that the outputs of simulations can be compared with the experimental data from the literature [33].
The aerodynamic field is compared via the $C_p - x/C$ curves, where C_p is the local pressure coefficient. The aim is to define the best angle of attack which replicates the experimental data from literature.

An important parameter to monitor as to ensure that the simulations are correct is y^+, which is the dimensionless wall distance. The value of y^+ must be near the value of 1 in each control volume of the airfoil; this requirement ensures that the first cell center is placed in the viscous sublayer, hence it is possible to capture the sublayer.

After the computation of the aerodynamic field, the next step is to retrieve the operative condition for the trajectory of the droplets and the computation of the collection efficiency β. In PoliDrop the input values for the simulations are related to the configuration of the clouds and the particles: the MVD, the extension of the cloud, the position of the cloud and the number of droplets; but they are also related to the simulation framework: the splash model employed, the total time of the simulation and the integration time-step. The aim is to perform a sort of convergence study on the β, used to define the best inputs to recreate the wind tunnel condition. Recalling from the case study that the MVD is fixed, the objective is accomplished by following this algorithm:

- Define the initial position of the cloud ahead of the airfoil in an unperturbed region of the domain;
- define a properly final simulation time in order to let the particles impinge the surface;
- set an integration time-step to obtain converged results;
- enable the splash and rebound of the droplets by setting the splash model.

The particle resolution is automatically adjusted by computing beta iteratively until the L_2 norm of the value of two successive iteration is below a given threshold.

3.3.3. Latin Hypercube Sampling (LHS)

As mentioned in Sec. 3.1, the method employed in this work to compute the coefficients of the PCE is a non-intrusive method with LS approach. Consequently, a set of deterministic realizations is needed, and the input values of these realizations are sampled with the Latin Hypercube Sampling (LHS) method.

LHS generates a near-random sample values from a multidimensional distribution. It is a generalization of the Latin Square to an arbitrary number of dimensions, inspired by the works of the Korean mathematician Choi Seok-Jeong and, afterwards, by Leonhard Euler. The LHS method, used in numerical simulations, was firstly described by McKay in 1979 [42].

Let $\mathbf{X} = \{X_1, ..., X_K\}$ be the K selected random input variables with known probability distribution $p(x)$, and let S be the sample space of $\mathbf{X}$; the idea is to partition S in strata to ensure that all portion of the space are sampled. Moreover, defining N as the number of samples, the range of each input variable X_k is divided into N strata of equal marginal probability $1/N$ and randomly sampled, once, from each stratum; this ensures that all the portions of the distribution of the input variables are represented by the input values extracted. Once all the N sample for each X_k are sampled, they are randomly combined. In this work the random inputs variables are 5 and they are shown together with their respective uniform distribution in Table 3.2 and Table 3.3; the number of sample is 224 for each variable and it is chosen in order to obtain 4 datapoints for each PCE coefficient. An additional set of 50 points, sampled with LHS as well, are computed to define a test set of realizations in order to assess the accuracy of surrogates

LHS is employed because it reduces the computational burden with respect to other sampling methods: indeed, a smaller number of samples is needed to obtain a precise statistical estimator [42].

Once the input values are sampled, the deterministic realizations of the model are computed by loosely coupling SU2 and PoliDrop. Due to the large siza of the simulation set, the simulations are run on Megamind, the computer cluster of CREALab at the Politecnico di Milano. Megamind is a Linux based remote server and it has 204 CPU cores units that can be fully exploited to execute parallel simulations. In this work the simulations for each case are performed in series but they are indipendent, therefore, they can be executed concurrently.

3.3.4. PCE

This section presents the algorithm applied to perform the LS fit for the PCE of the collection efficiency which is computed on each element of the surface mesh.

The first step is to retrieve the points and the connectivity of the surface elements. The next step consists in reading the parameters of the sampled point from the file output of the LHS algorithm. The input values are expressed as the variance between the sampled and the nominal values, both multiplied by two and normalized with the interval of respective uniform distribution. This passage renders the different parameters comparable to each other; indeed now the data set can only have values belonging to the interval $[-1, 1]$.

The coefficients are computed employing the LS approach; the Z matrix defined in Eq. 3.17 is computed by defining a multivariate function in Matlab derived from the computation of the first four polynomial of Legendre, using the normalized sampled values; the polynomials are chosen in accordance with the Table 3.1 and the order of the PCE.

At this point, read the output of each deterministic realizations has to be read and it is possible to compute the upper and lower impingement limits, where β is equal to 0. The aim is to get rid of the panels where water is never collected in any simulations, in order to reduce the surrogates to model and, consequently, to reduce the computational burden.

Once the collection efficiency and the matrix Z are available, it is possible to perform the LS approach; in Matlab, this can be done with the function `mldivide(Z,y)` which returns the least-square solution of the system $Z * c = y$, i.e. the matrix that contains the PCE coefficients.

To validate the surrogates of the model, the Root Mean Square Error (RMSE) is computed by comparing PC prediction against the deterministic realizations of testing data set. The expected value, the variance and the Sobol indices are straightforward computed manipulating the vector containing the PCE coefficients. The results of the stochastic analysis will be presented in the next chapter.

4 | Simulations and results

Being the cases studied in this work real, they have uncertainties; therefore, the aim is to propagate them on the simulations. In this chapter the collection efficiency β numerical results is analyzed in both airfoils taken into account.

This chapter is divided in a first section where the results of the grid convergence study are presented; and two sections related to the two different airfoil studied. The latters section are divided in a first part where the results of the nominal condition are presented; and a second one where the UQ study is discussed. For the NACA-23012 case, the UQ study is split in the Appendix-C and Appendix-O to better present the results and the comparison between both cases.

4.1. Preliminary study

As mentioned in Sec 3.3, the first step of the work is to define the better choice for the mesh. In Fig. 4.1, the grid convergence study is shown.

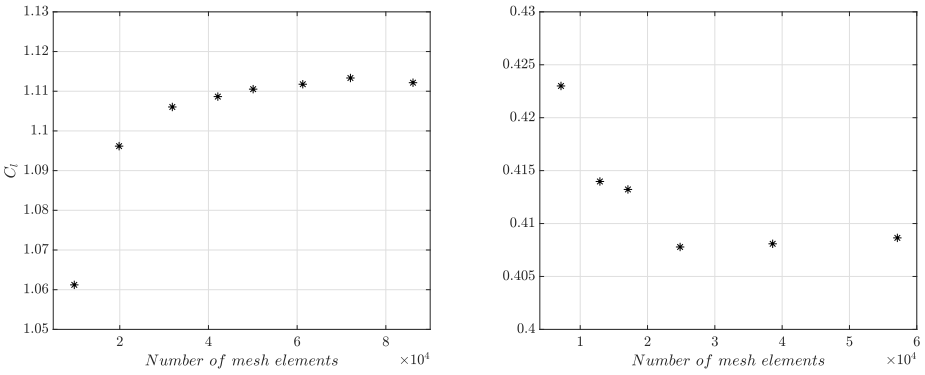

(a) MS(1)-317 (b) NACA-23012

Figure 4.1: Grid convergence

In accordance with Fig. 4.1 the mesh selected for the study on MS-137 airfoil has 42116 elements, while for the study of NACA-23012, the mesh is composed of 34529 elements.

In Fig. 4.2, it is possible to note that y^+ is around 1 for each control volume along the surface meaning that the meshes are well defined and they are able to catch the sublayer.

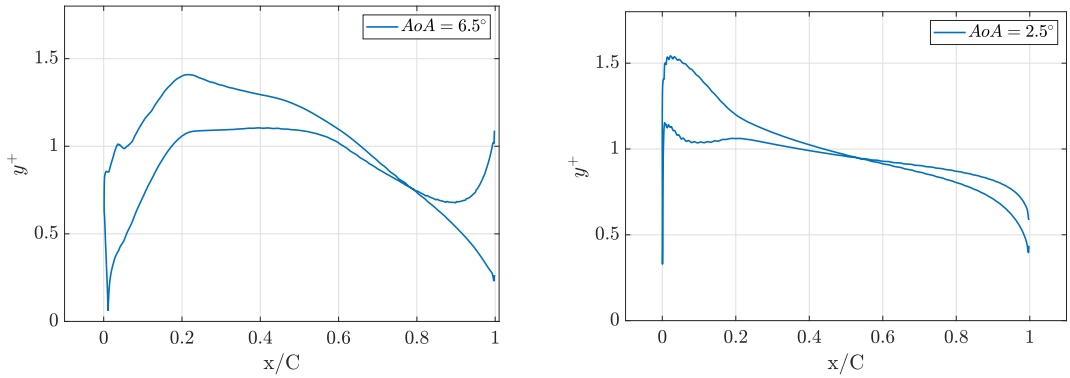

(a) MS-317 (b) NACA-23012

Figure 4.2: y^+ curves.

4.2. MS-317

4.2.1. Replicate test condition

From Fig. 4.3 the curve that better fits the experimental data is the one related to 6.5^o. The reason for the different AoA between the computational case and the experimental setup is due to the wind tunnel calibration.

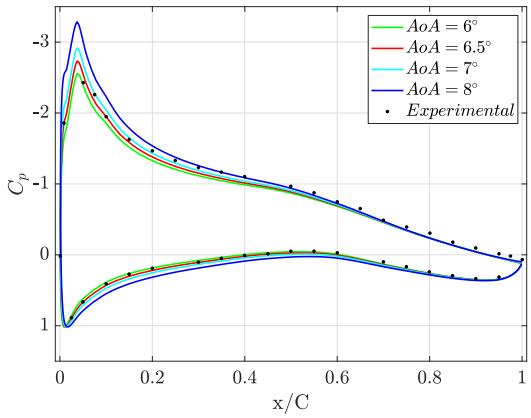

Figure 4.3: C_p over the curvilinear abscissa curves comparison. MS-317 case.

In Fig. 4.4, the results of this work for the nominal case for the collection efficiency are presented in comparison with the experimental data from the literature [33]. It is possible to note that when the splash model is employed, the curve obtained has a good overlap with the experimental data.

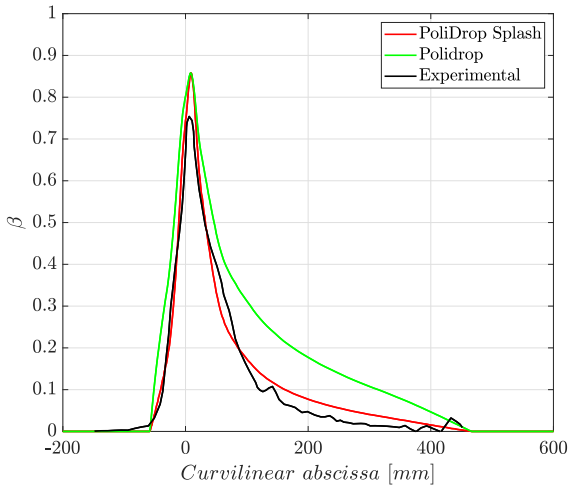

Figure 4.4: Collection efficiency's nominal case. MS-317 case.

4.2.2. UQ study

Fig. 4.5 shows the surrogates assessment and, in particular, the mean β obtained by the first coefficient of the PC expansion computed, together with the Root Mean Square error calculated with respect to collection efficiency output of the 50 additional sampled set which was mentioned in Sec. 3.3. Both results are plotted w.r.t. the curvilinear abscissa of the airfoil: the origin is the Leading Edge (LE) and it is positive counterclockwise.

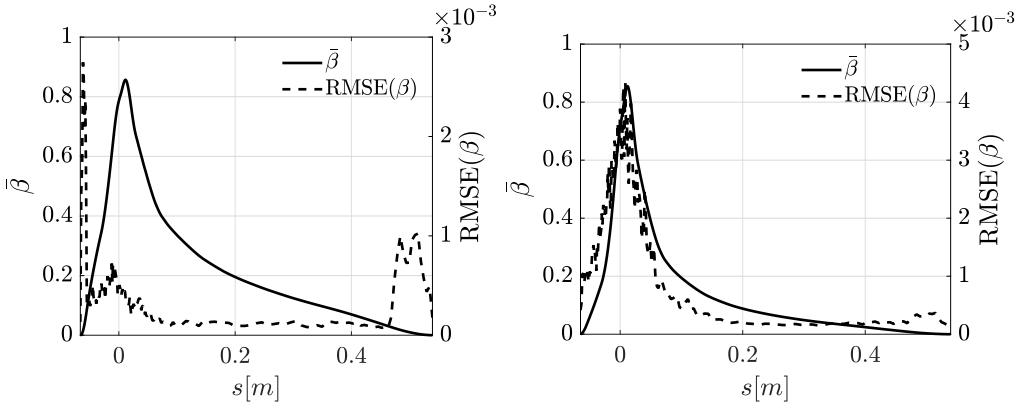

(a) No splash model employed. (b) LEWICE splash model employed.

Figure 4.5: Mean β (left scale) and RMSE (right scale) of PC predictions.

The maxima RMS errors are, respectively, in Fig. 4.5(a) in the region of impingement limits, marked as grey area in Fig. 4.7; and in Fig. 4.5(b) in the area of the LE. For both cases, the PCE is a good prediction because the maxima RMSE is below 1% of the bulk coefficiton efficiency.

Fig. 4.6 shows the comparison between the numerical prediction and experimental data. The red shaded areas are obtained by adding twice the standard deviation (2σ) to the

$\bar{\beta}$ computed; 2σ is defined as the uncertainty bound of the numerical output and the standard deviation is computed as the square root of the variance σ^2, which is a result of manipulating the PCE coefficients.

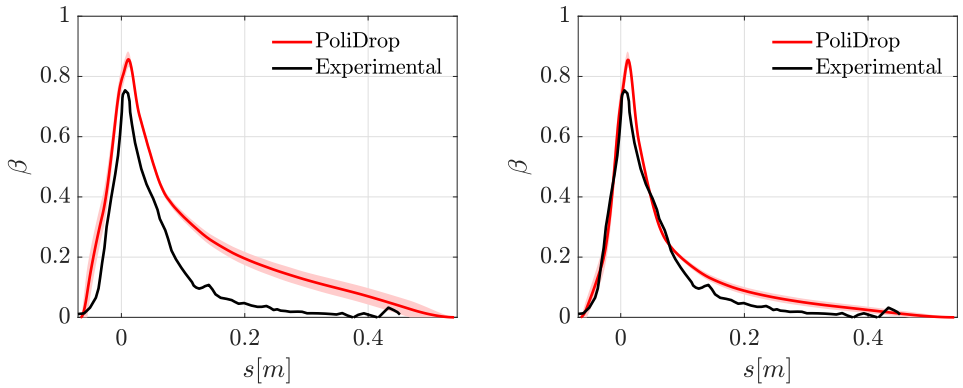

(a) No splash model employed. (b) LEWICE splash model employed.

Figure 4.6: Comparison among numerical prediction and experimental data.

The curve shows a good overlap with the experimental data in the case where the LEWICE splash model is employed (Fig. 4.6(b)); on the contrary, the curve of Fig. 4.6(a) is not a good overlap, especially in the LE and in the upper surface. This behaviour is expected, since in this case the MVD is equal to 92 μm; being larger than 40 μm, it must be related to SLD and appendix-O conditions.

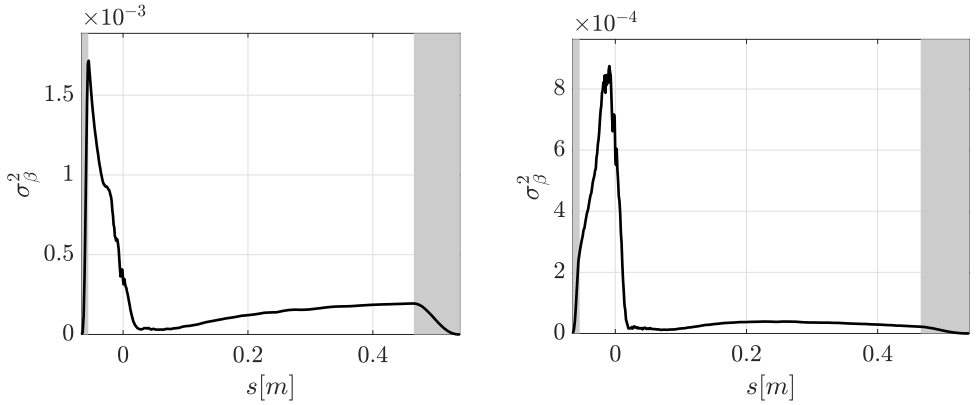

(a) No splash model employed. (b) LEWICE splash model employed.

Figure 4.7: Variance decomposition and impingement limits.

The variance decompositions w.r.t. the curvilinear abscissa are shown in Fig. 4.7: for the case where the LEWICE splash model is employed, the peak of the variance is in the region of the LE, then it rapidly decreases on the pressure side of the airfoil and remains almost constant to a much lower value than the peak; however, on the suction side, the variance increases almost linearly from the impingement limit to the peak of the curve. In Fig. 4.7(a), instead, the maxima of the variance are in the region of the impingement

limits and the absolute maximum is in suction side of the airfoil, where, in the test data set, the collection efficiency is often near or equal to 0. It is also possible to notice that the variance throughout the airfoil is one order of magnitude lower than in the case where the splash model is employed. This behaviour can be explained by the fact that the latter can better replicate the physics of the problem, it is also important to remember that the starting data are taken from real tests conducted in a wind tunnel and the aim of the numerical simulations is to reproduce that values of collection efficiency.

The Sobol indices decompositions, normalized by the local value of the variance, are presented in Fig. 4.8 w.r.t. the curvilinear abscissa of the airfoil. They show the local dependence of the random parameters on the variance, and therefore which random input contributes the most to the uncertainty of the output. It is possible to note that in the case in which the splash model is not employed, the purple area is predominant, meaning that MVD contributes the most on the variance throughout the surface. On the other hand, where the LEWICE splash model is employed, it is possible to note the most contributing parameter is the AoA in the area near the LE and on the pressure side. The reason for this difference depends the angle of impact of the droplets, which is an important parameter to define the splash or rebound of the particle; moreover the difference is placed on the pressure side of the airfoil due to the positive AoA and the camber of the surface. Table 4.1 shows the integrate values of the Sobol indices: they are normalized over the integral value of the variance of β and the table gives an idea of which parameter contributes the most on the uncertainty of the whole airfoil. Indeed, it is possible to note that in both cases the parameters have almost the same incidence, and MVD contributes the most to the variance. Moreover, the AoA increases its incidence on the total variance in the case where the splash model is employed, but not as much as can be expected from Fig. 4.14(b); this happens is because the majority of the variance is in the suction side of the airfoil, as it is possible to see in Fig. 4.13(b).

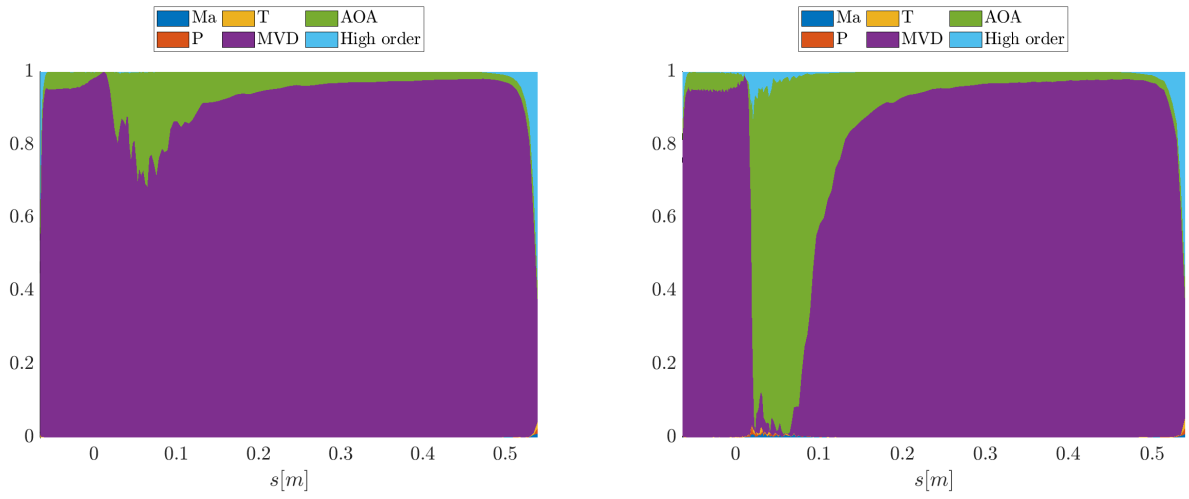

(a) No splash model employed.

(b) LEWICE splash model employed.

Figure 4.8: Variance decomposition in first order sobol indices.

	Mach	Pressure	Temperature	MVD	AoA	Higher Order
No Splash	0.0048%	0.0039%	0.0048%	95.5290%	4.2813%	0.1763%
Splash	0.0248%	0.0277%	0.0238%	93.7796%	5.7682%	0.3758%

Table 4.1: Integral values of Sobol indices normalized by the total variance of β

4.3. NACA-23012

This section is divided in three parts: in the first one, the results related to the nomimal condition will be shown; in the second one, to the appendix-C conditions will be presented; in the last one, the results related to the SLD cases, i.e. for larger MVD, will be shown.

4.4. Replicate test condition

For the NACA-23012 case, it is possible to note in Fig. 4.9(a) and in its enlargement (Fig. 4.9(b)) that a larger AoA, which in the specific example is equal to 2.9^o, better reproduces the experimental pressure coefficient on the upper surface of the airfoil w.r.t. to an AoA equal to 2.5^o; however, a larger AoA also produces a worsening on the lower surface. On the contrary, a smaller AoA, such as equal to 2.1^o, shows the opposite behaviour. For these reasons, in the work an AoA of 2.5^o will be employed.

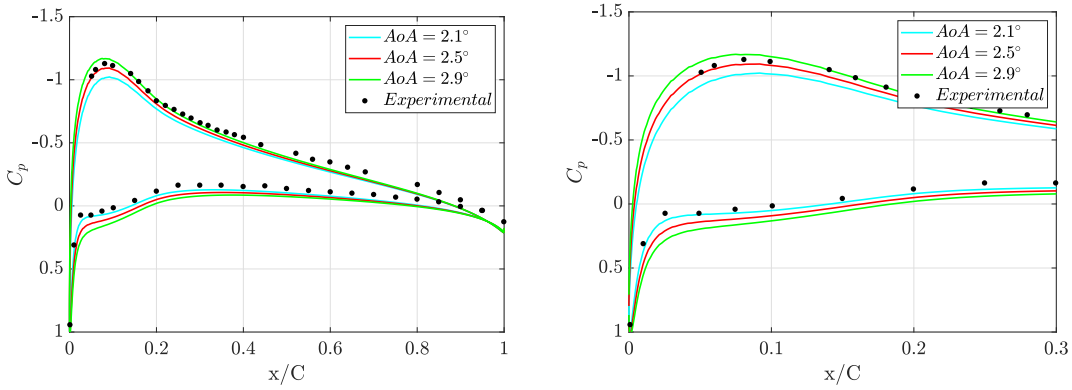

(a) (b) Zoom on (a)

Figure 4.9: $C_p - x$ curves for different angle of attack compared with the experimental data from [33]. NACA-23012 case.

Fig. 4.9 shows the collection efficiency obtained with PoliDrop using the nominal condition as input variables. As expected, for SLD cases, β obtained employing the LEWICE splash model better fits the experimental data. When MVD is equal to $20\,\mu$m, instead, the two curves nearly overlap.

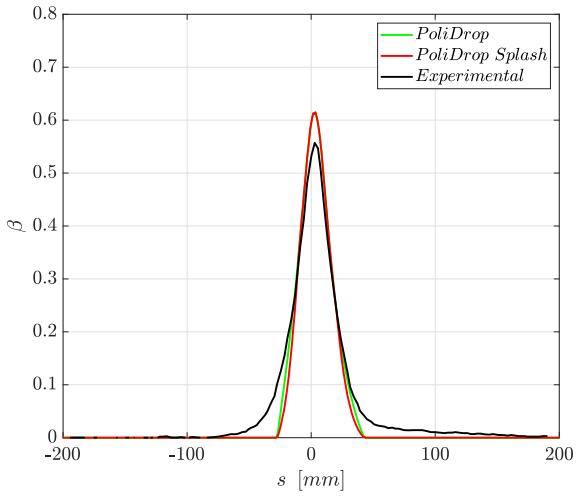

(a) $MVD = 20\,\mu$m

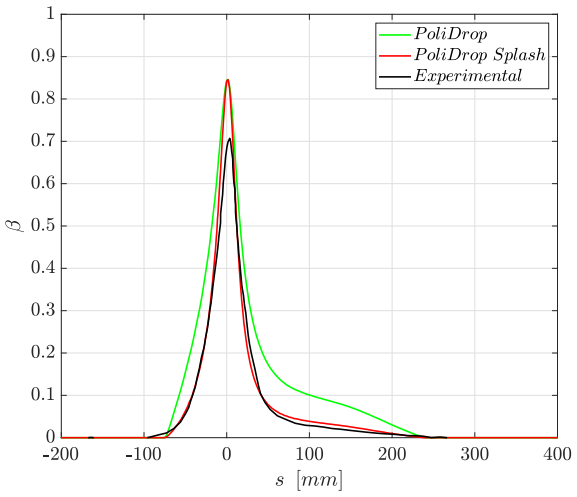

(b) $MVD = 52\,\mu$m

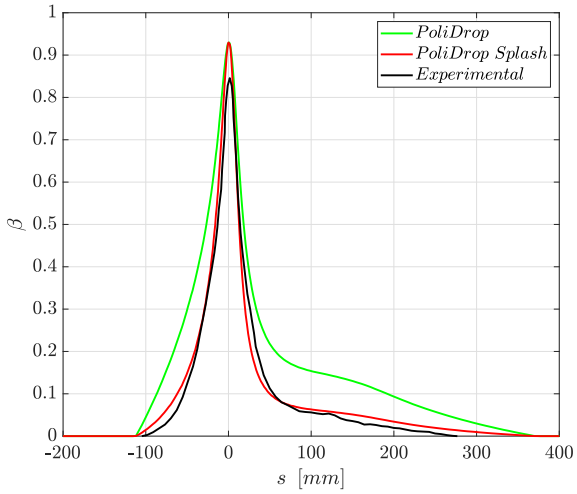

(c) $MVD = 111\,\mu$m

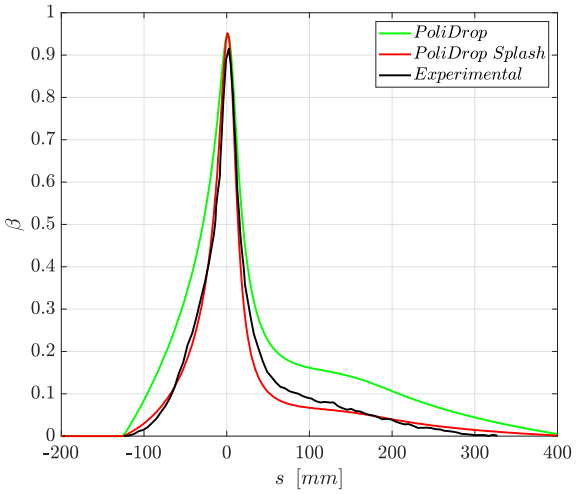

(d) $MVD = 154\,\mu$m

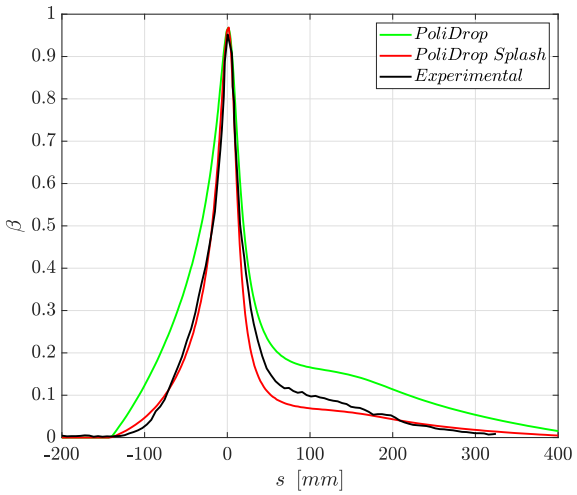

(e) $MVD = 236\,\mu$m

Figure 4.10: Collection efficiency's nominal case. NACA-23012 case.

4.4.1. UQ study for Appendix-C condition

As for the MS-317 case, all the results are plotted over the curvilinear abscissa of surface. Fig. 4.11 shows the mean collection efficiency $\bar{\beta}$ obtained by the study of the PCE coefficients of the surrogates modelled. The dashed line is related to the RMSE of the PC prediction which is computed w.r.t. the test data set: it is possible to note that the curve has two peaks in rthe region of the impingement limits, which are the grey area of Fig. 4.13; however, the maximum RMSE is below 1% of the bulk β so that the PCE can be considered a good prediction of the collection efficiency.

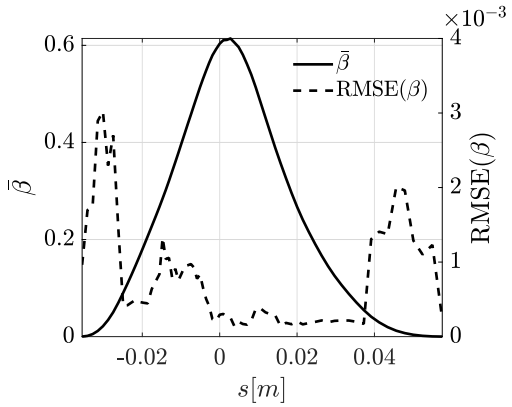

Figure 4.11: Mean β (left scale) and RMSE (right scale) of PC predictions.

The comparison among numerical results and experimental data (Fig. 4.12) shows a moderate overlap considering $\bar{\beta}$, while a better overlap is shown considering the red shaded area; this corresponds to the uncertainty bound of the mean β, computed as twice the standard deviation.

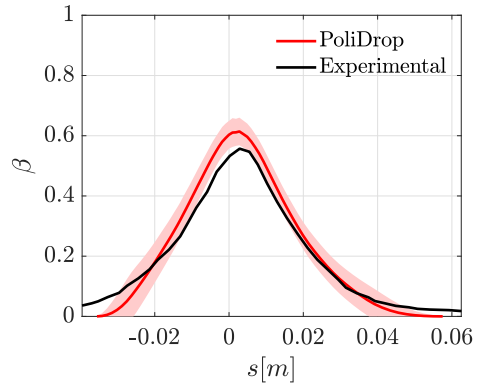

Figure 4.12: Comparison among numerical prediction and experimental data.

The variance decomposition curve, Fig 4.13, has two maxima in the region of the impingement limits, the grey areas, and a minimum near the leading edge: this behaviour is due to the positive angle of attack and characteristic when the splash model is not employed.

Considering the sensitivity analysis, i.e. the Sobol indices shown in Fig. 4.14, it is possible to note that the uncertainty on the MVD is prevalent along the curvilinear abscissa; this

is true also taking in to accout the integral values of Table 4.2. Moreover, the latter shows that, in this case, the AoA contributes more than in MS-317 case.

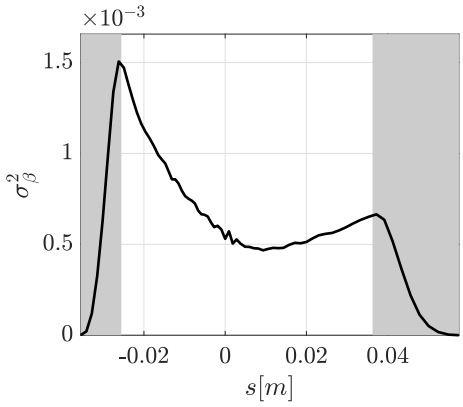

Figure 4.13: Variance decomposition and impingement limits.

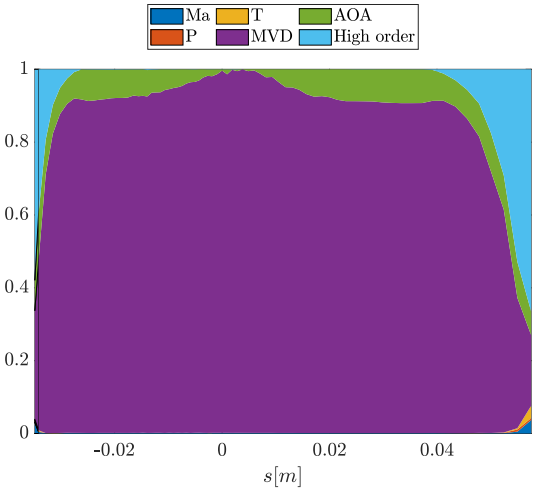

Figure 4.14: Variance decomposition in first order Sobol indices.

Mach	Pressure	Temperature	MVD	AoA	Higher Order
0.1465%	0.0040%	0.0069%	92.9306%	7.0786%	1.0068%

Table 4.2: Integral values of Sobol indices normalized by the total variance of β

4.4.2. UQ study for Appendix-O condition

In this section, the results on the Appendix-O condition for the NACA-23012 will be presented and compared with the Appendix-C condition.

Fig. 4.15 shows the mean collection efficiency: it is interesting to note that the maximum of the solid line increases when MVD increases; this behaviour is expected in accordance

with the experimental data, as shown in Fig. 4.16. In the latter figure, the comparison also shows that the overlap between the red and black curve increases when MVD increases; for MVD equal to $236\mu m$, the PC prediction is remarkably accurate w.r.t. experimental data. The uncertainty bounds of the red curve, highlighted with the red shaded area, becomes less notable as the median diameter of the particle increase, also in comparison with the previous case regarding the appendix-C condition (Fig. 4.12). This demonstrates that increasing MVD, the precision of the surrogate prediction increases. Only for MVD equal to $52\,\mu$m and $111\,\mu$m, the peak of the collection efficiency appears to be overestimated.

The trend of a better approximation increasing the diameter, is also confirmed by looking at the maximum of the curves of the variance decomposition (Fig. 4.17). Indeed, they decrease because particles with larger diameter are less perturbed by the flow field due to the larger Stokes number; the numerical outputs depend on geometrical parameters and particle trajectory, so that considering larger droplets, the uncertainties on the geometry has a milder impact on the collection efficiency.
It's important to highlight that the trend of the variance curves is similar to the one for MVD larger than $40\mu m$: starting from the impingement limit on the suction side, σ^2 increases almost linearly until the peak, located in the region of the leading edge; then, it rapidly decreases to a value that remains almost constant throughout the pressure side. However, this trend is extremely different w.r.t. the variance's curve of the appendix-C case (Fig 4.13).

The Sobol indices also have a different distribution throughout the airfoil w.r.t. the $20\mu m$ case: on the upper part of the surface, the behaviour is almost constant at different diameter; on the contrary, at lower surface, the AoA has an increasing relevance when the diameter increases, as shown by the green area in Fig. 4.18. This incresing relevance is also highlighted by Table 4.3. This is due to the fact that for larger droplets, the angle of attack and the angle of impingement of the particle play an important role on the physics and. therefore, also on the model employed; they are, indeed, two of the parameters governing the splash of the droplets. As mentioned before, if the impact angle tends to be normal to the surface, the droplets splash. However, in accordance with Table 4.3, the most of the uncertainty on the output is due to MVD, since it is still more relevant than the other parameters in the suction side of the airfoil, which is the area with larger values of variance. This can be explained by the positive angle of attack and the camber of the airfoil.

	Mach	Pressure	Temperature	MVD	AoA	Higher Order
MVD=52 μm	0.0615%	0.0046%	0.0024%	82.7863%	19.8405%	0.1720%
MVD=111 μm	0.0097%	0.0023%	0.0029%	89.5360%	11.4417%	0.1017%
MVD=154 μm	0.0077%	0.0035%	0.0035%	86.0803%	15.1185%	0.1165%
MVD=236 μm	0.0077%	0.0088%	0.0187%	77.9539%	23.7944%	0.1898%

Table 4.3: Integral values of Sobol indices normalized by the total variance of β

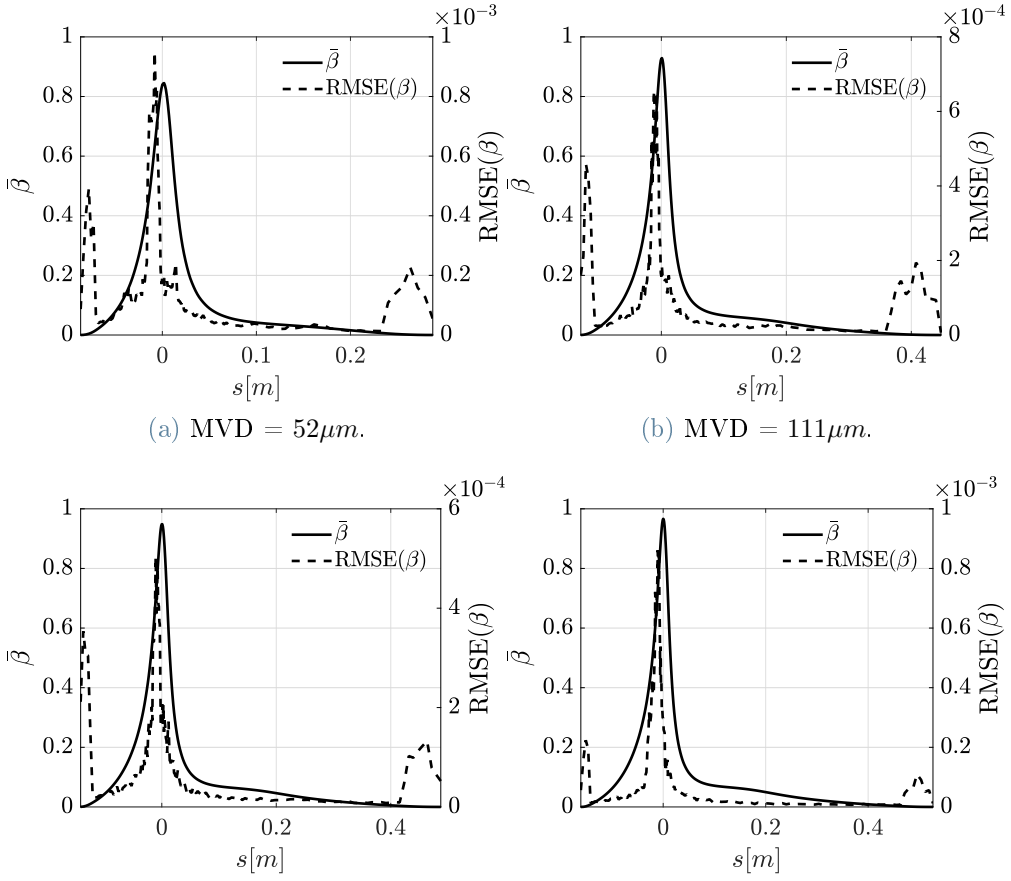

(a) MVD = 52μm.

(b) MVD = 111μm.

(c) MVD = 154μm.

(d) MVD = 236μm.

Figure 4.15: Mean β (left scale) and RMSE (right scale) of PC predictions.

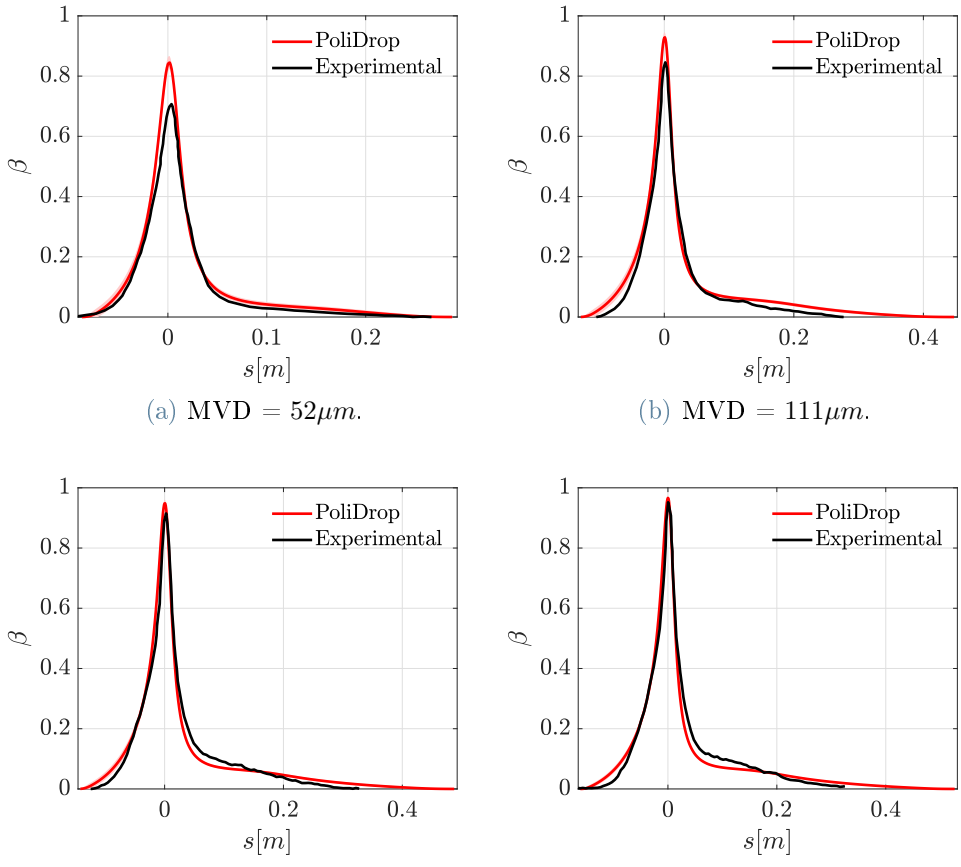

(a) MVD = 52μm. (b) MVD = 111μm.

(c) MVD = 154μm. (d) MVD = 236μm.

Figure 4.16: Comparison among numerical prediction and experimental data.

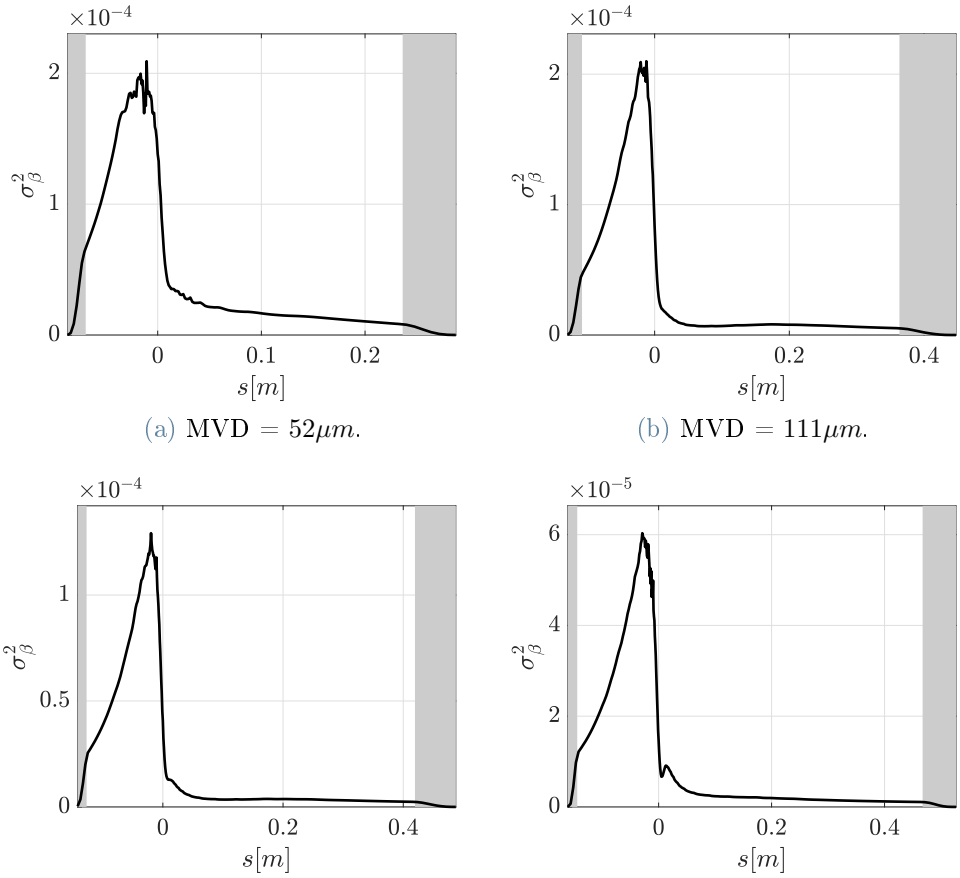

(a) MVD = 52μm. (b) MVD = 111μm.

(c) MVD = 154μm. (d) MVD = 236μm.

Figure 4.17: Variance decomposition and impingement limits.

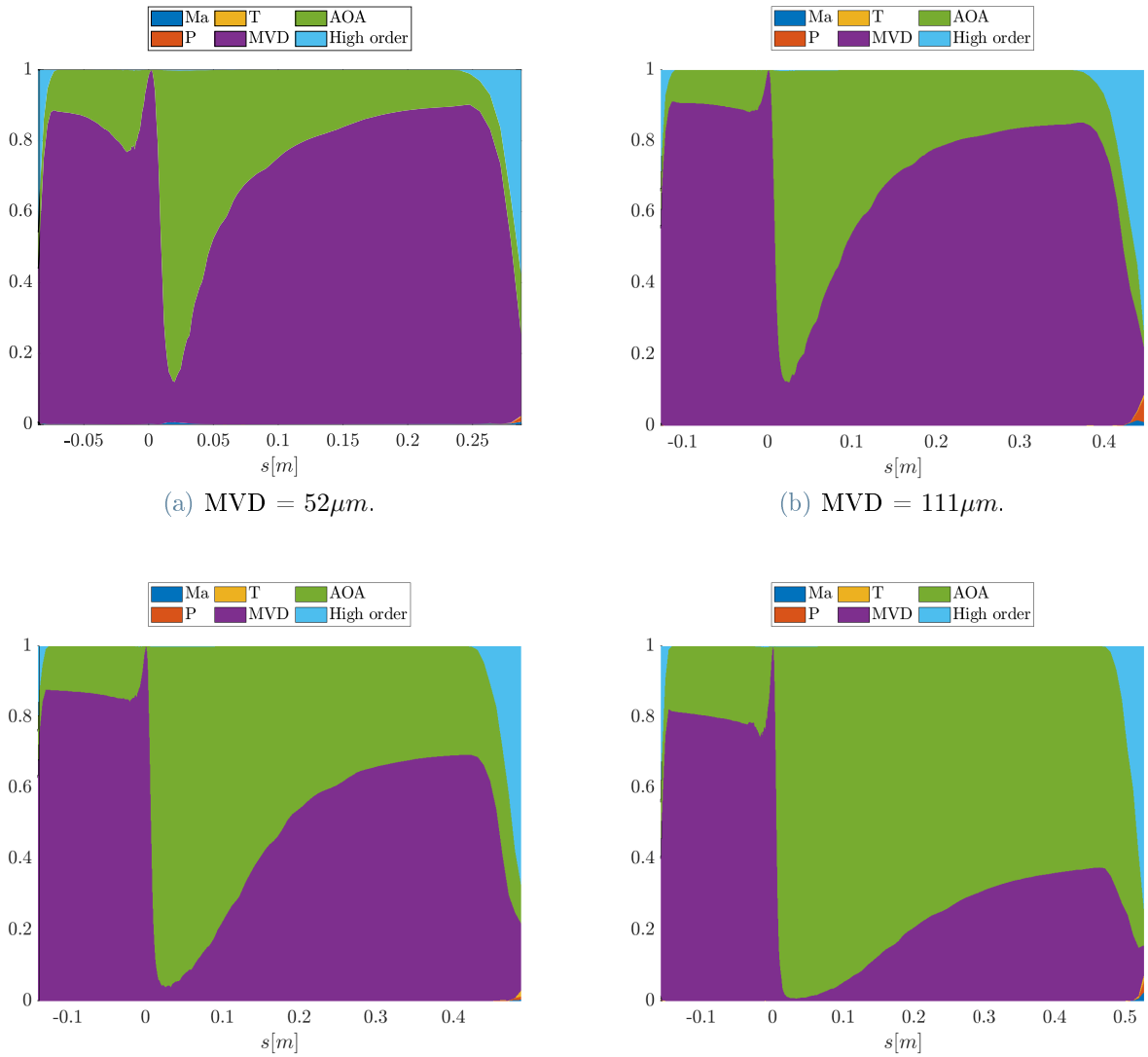

(a) MVD = $52\mu m$.

(b) MVD = $111\mu m$.

(c) MVD = $154\mu m$.

(d) MVD = $236\mu m$.

Figure 4.18: Variance decomposition in first order Sobol indices.

5 | Conclusions and future developments

This thesis presented a computational framework to compute the collection efficiency under uncertainty. The in-house Lagrangian particle tracking code PoliDrop is coupled with the open-source CFD solver SU2 to calculate the aerodynamic field and the collection efficiency β. The uncertainties of the random input variable is propagated through the entire computational model using a PC approach in order to define the uncertainty bounds of the numerical output. This process is applied using two different two-dimensional geometries, however, it can also be employed to any geometrical problem, and even three-dimensional cases.

The numerical outputs are preliminary compared with the experimental data collected at NASA IRT and described in [33]. The simulations fairly reproduce any case presented, demonstrating the capability of the computational framework to predict the experimental observations.

The stochastic analysis is performed by computing and manipulating the PCE coefficients obtained. The analysis shows different, yet similar behaviour between the cases proposed. Considering the MS-317 airfoil a comparison among employing or not a splash model to the particle tracking software is done. When the LEWICE splash model is employed, the PC prediction better replicates the experimental data; moreover, the variance is one order of magnitude smaller than the case where the assumptions described in Sec. 2.2 are implemented. This behaviour was expected due to the physics of the problem, which is better approximated by applying a splash model to PoliDrop, since the MVD of this case is larger than $40\,\mu$m, therefore lying in the Appendix-O conditions.
The variance curves also show different characteristics: where the splash model is employed, the maximum of the curve is in the region of the LE, while in the suction side of the airfoil it decreases almost linearly until the impingement limit; on the other hand, the curve has the peak at the impingement limit on the upper part of the surface, then it decreases until a minimum in the neighborhood of the LE and it slightly increases to a new maximum at the impingement limit in the lower part of the surface.
The sensitivity analysis is obtained by studying the first Sobol indices: the major contribution to the variance in both cases is due to the uncertainty on the MVD, and furthermore, the relevance of the AoA increases when the splash model is used, especially near the LE in the pressure side of the airfoil. The other random parameters have much lower influence on the uncertainty and, therefore, can be neglected in future analysis.

Considering the NACA-23012, the uncertainty quantification study is performed increasing the diameter of the particles, while comparing the collection efficiency results for Appendix-C and Appendix-O conditions. The variance shows different behaviour between these cases: in the Appendix-C condition, the curve has two peaks in the impingement limit and a minimum at the LE; for MVD greater than $40\,\mu$m, the curves increase from the impingement limit on the suction side of the airfoil until the maximum near the LE, then rapidly decrease to a value which remains almost constant throughout the pressure side of the surface. Moreover, considering the SLD cases, the collection efficiency presents a more prominent peak and longer tails when MVD increase; furthermore, the impingement limits move further aft, in a manner which is directly proportional to the MVD.
Concerning the Sobol indices, in each case taken into account the major contribution to the uncertainty is related to the MVD. However, it is important to highlight that in Appendix-C conditions, the uncertainty on the cloud contributes likewise along the surface. In the SLD cases, instead, the indices exhibit a different composition on the suction and on the pressure side of the airfoil: in the suction side, where the variance is larger, the most contributing parameter is the MVD; in the pressure side, where the variance is smaller, AoA increases its contribution as the particle diameter increases. The other parameters considered can be neglected in future works due to their minimal contribution on the uncertainty of the output.

The main objective of this thesis was to propagate the experimental uncertainty through the entire computational framework in order to compute the collection efficiency. The results, compared with the experimental data, give important insights about the validity of the code and they demonstrate that assessing the input uncertainties is fundamental to retrieve the experimental condition. However, the reasons for the overestimated peaks of β in some Appendix-O cases are not related to the experimental setup and they must be investigated in numerical models, such as the drag coefficient model or the particle break up.
Considering the sensitivity analysis it is possible to extract another important information: the MVD is the most contributing parameter to the uncertainty of the collection efficiency; however, the AoA increases its inlfluence when the diameter of the particles increases. This insight can be useful for future tests setup in the wind tunnel or in the design of the IPS.

In this work the uncertain parameter are related to the experimental setup; a possible future development could aim at fully characterizing the sources of uncertainty, such as the empirical model of the particle break up, or the C_D-Re model. This would lead to a complete definition of the sources of uncertainty in the SLD model of the physics and, consequently, in the numerical simulations.

References

[1] Lynch, Frank T., and Abdollah Khodadoust. *Effects of ice accretions on aircraft aerodynamics.* Progress in Aerospace Sciences 37.8 (2001): 669-767.

[2] Baars, Woutijn J., Ronald O. Stearman, and Charles E. Tinney. *A Review on the Impact of Icing on Aircraft Stability and Control.* Journal of Aeroelasticity and Structural Dynamics 2.1 (2010).

[3] Lou, Decang, and David W. Hammond. *Heat and mass transfer for ice particle ingestion inside aero-engine.* (2011): 031021.

[4] Bragg, Michael B., Andy P. Broeren, and Leia A. Blumenthal. *Iced-airfoil aerodynamics.* Progress in Aerospace Sciences 41.5 (2005): 323-362.

[5] Carroll TC, McAvoy WH. *Formation of ice on airplanes.* Airway Age, September 1928. p.58–9

[6] Aircraft Icing. NASA Conference Publication 2086 or FAA-RD-78-109, July, 1978

[7] AIN online: https://www.ainonline.com/aviation-news/

[8] Stefan, J., *Ueber die theorie der eisbil-dung im polarmeere.* Annalen Der Physik Und Chemie, Vol. 42, 1891, pp. 269–286.

[9] Messinger, B. L., *Equilibrium Temperature of an Unheated Icing Surface as a Function of Air Speed.* Journal of the Aeronautical Sciences, Vol. 20, No. 1, 1953, pp. 29–42.

[10] DeGennaro, Anthony M., Clarence W. Rowley, and Luigi Martinelli. *Uncertainty quantification for airfoil icing using polynomial chaos expansions.* Journal of Aircraft 52.5 (2015): 1404-1411.

[11] Raj, L. Prince, K. Yee, and R. S. Myong. *Sensitivity of ice accretion and aerodynamic performance degradation to critical physical and modeling parameters affecting airfoil icing.* Aerospace Science and Technology 98 (2020): 105659.

[12] Feng, Kaixuan, Zhenzhou Lu, and Wanying Yun. *Aircraft icing severity analysis considering three uncertainty types.* AIAA journal 57.4 (2019): 1514-1522.

[13] Gori, G., Congedo, P. M., Le Maître, O., Bellosta, T., & Guardone, A. (2021). *Modeling In-Flight Ice Accretion Under Uncertain Conditions.* Journal of Aircraft, 1-15.

[14] Bellosta, Tommaso, et al. *Uncertainty quantification for in-flight ice accretion under Appendix-C and Appendix-O conditions.* AIAA Aviation 2021 Forum. 2021.

[15] Cebeci, Tuncer, and Fassi Kafyeke. *Aircraft icing.* Annual review of fluid mechanics 35.1 (2003): 11-21.

[16] SU2. The Open-Source CFD code. https://su2code.github.io/

[17] Bourgault, Yves, et al. *A finite element method study of Eulerian droplets impingement models.* International Journal for Numerical methods in fluids 29.4 (1999): 429-449.

[18] Gent, Roger W., Nicholas P. Dart, and James T. Cansdale. *Aircraft icing.* Philosophical Transactions of the Royal Society of London. Series A: Mathematical, Physical and Engineering Sciences 358.1776 (2000): 2873-2911.

[19] Clift, Roland, John R. Grace, and Martin E. Weber. *Bubbles, drops, and particles.* (2005).

[20] Code of Federal Regulations. 14 CFR 25.1419-1420, Revised as of Nov. 4, 2014.

[21] Hu, Tao, et al. *Study on airworthiness problems of operating in supercooled large drops icing conditions for transport category airplanes.* Procedia Engineering 80 (2014): 467-478.

[22] Kékesi, Timea, Gustav Amberg, and L. Prahl Wittberg. *Drop deformation and breakup.* International Journal of Multiphase Flow 66 (2014): 1-10.

[23] Honsek, Raimund, and Wagdi G. Habashi. *FENSAP-ICE: Eulerian modeling of droplet impingement in the SLD regime of aircraft icing.* 44th AIAA aerospace sciences meeting and exhibit. 2006.

[24] Wright, William. *Further refinement of the LEWICE SLD model.* 44th AIAA Aerospace Sciences Meeting and Exhibit. 2006.

[25] Papadakis, M., Elangonan, R., Freund, Jr., G. A., Breer, M., Zumwalt, G. W. and Whitmer, L., *An Experimental Method for Measuring Water Droplet Impingement Efficiency on Two- and Three-Dimensional Bodies.* NASA CR–4257, Nov. 1989

[26] Papadakis, M., Breer, M., Craig, N. and Liu, X., *Experimental Water Droplet Impingement Data on Airfoils, Simulated Ice Shapes, an Engine Inlet and a Finite Wing.* NASA CR–4636, DOT/FAA/CT–TN93/18, Dec. 1994

[27] Papadakis, M., Hung, K.E., Vu, G.T., Yeong, H.W., Bidwell, C.S., Breer, M.D., Bencic, T.J., *Experimental Investigation of Water Droplet Impingement on Airfoils, Finite Wings, and an S-Duct Engine Inlet.* NASA/TM—2002-211700, Oct. 2002

[28] Mundo, C. H. R., M. Sommerfeld, and C. Tropea. *Droplet-wall collisions: experimental studies of the deformation and breakup process.* International journal of multiphase flow 21.2 (1995): 151-173.

[29] Mundo, C. H. R., C. Tropea, and M. Sommerfeld. *Numerical and experimental investigation of spray characteristics in the vicinity of a rigid wall.* Experimental thermal and fluid science 15.3 (1997): 228-237.

[30] Mundo, C. H. R., Martin Sommerfeld, and Cameron Tropea. *On the modeling of liquid sprays impinging on surfaces.* Atomization and sprays 8.6 (1998).

[31] McGhee, Robert J. *Low-speed aerodynamic characteristics of a 17-percent-thick medium speed airfoil designed for general aviation applications.* National Aeronautics and Space Administration, Scientific and Technical Information Branch, 1980.

[32] Menter, Florian R. *Two-equation eddy-viscosity turbulence models for engineering applications.* AIAA journal 32.8 (1994): 1598-1605.

[33] Papadakis M, Rachman A, Wong S, Yeong H, Hung K, Vu G, Bidwell C. *Water droplet impingement on simulated glaze, mixed, and rime ice accretions* NASA Report, TM-2007-213961, Kansas, 2007

[34] Soeder, R.H., Sheldon, D.W., Ide, R.F., Spera, D.A., and Andracchio, C.R., *NASA Glenn Icing Research Tunnel User Manual* National Aeronautics and Space Administration, Glenn Research Center, NASA/TM—2003-212004, September 2003.

[35] Wiener, Norbert. *The homogeneous chaos.* American Journal of Mathematics 60.4 (1938): 897-936.

[36] Cameron, Robert H., and William T. Martin. *The orthogonal development of nonlinear functionals in series of Fourier-Hermite functionals.* Annals of Mathematics (1947): 385-392.

[37] Xiu, Dongbin, and George Em Karniadakis. *The Wiener-Askey polynomial chaos for stochastic differential equations.* SIAM journal on scientific computing 24.2 (2002): 619-644.

[38] Sobol, Ilya M. *Global sensitivity indices for nonlinear mathematical models and their Monte Carlo estimates.* Mathematics and computers in simulation 55.1-3 (2001): 271-280.

[39] Crestaux, Thierry, Olivier Le Maître, and Jean-Marc Martinez. *Polynomial chaos expansion for sensitivity analysis.* Reliability Engineering & System Safety 94.7 (2009): 1161-1172.

[40] Anderson, David N., and Jen-Ching Tsao. *Ice shape scaling for aircraft in SLD conditions* No. NASA/CR-2008-215302. 2008.

[41] Dussin, D., Fossati, M., Guardone, A., and Vigevano, L. (2009). *Hybrid grid generation for two-dimensional high-Reynolds flows.* Computers & fluids, 38(10), 1863-1875.

[42] McKay, M. D., and R. J. Beckman. *A Comparison of Three Methods for Selecting Values of Input Variables in the Analysis of Output From a Computer Code* Technometrics: A journal of statistics for the physical, chemical and engineering sciences 42.1 (2000): 55.

Ringraziamenti

Al termine di questo lavoro di tesi vorrei ringraziare le persone che a vario titolo hanno reso possibile il mio percorso al Politecnico di Milano.
Innanzitutto ringrazio il Professor Alberto Guardone per avermi dato la possibilità di approfondire un tema importante e stimolante come l'accrescimento del ghiaccio. Insieme ringrazio Tommaso per l'enorme aiuto durante il lavoro di tesi.
Un grazie alla mia famiglia, in particolare i miei genitori, che hanno sempre appoggiato le mie scelte, le hanno rese possibili e mi hanno supportato e sopportato, in particolar modo durate gli anni universitari.
Un grazie enorme agli amici di sempre Claudio e Daniele, tutti dovrebbero poter avere amici come loro. Grazie a tutte le persone conosciute in università, in particolar modo Filippo, Antonio, Lorenzo, Riccà, l'Andre del Tonale e Bez senza i quali l'università non sarebbe stata la stessa.
Infine vorrei ringraziare Sofia, semplicemente senza di lei sarebbe stato impossibile essere qua. A lei è dedicato questo lavoro.